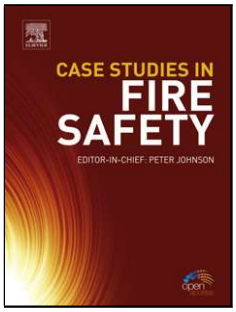

Title: Smart-release inhibition of corrosion driven organic coating failure on zinc by cationic benzotriazole based pigments

Authors: C.A.J. Richards, H.N. McMurray, G. Williams

PII: S0010-938X(19)30053-8
DOI: https://doi.org/10.1016/j.corsci.2019.04.005
Reference: CS 7971

To appear in:

Received date: 7 January 2019
Revised date: 2 April 2019
Accepted date: 7 April 2019

Please cite this article as: Richards CAJ, McMurray HN, Williams G, Smart-release inhibition of corrosion driven organic coating failure on zinc by cationic benzotriazole based pigments, *Corrosion Science* (2019), https://doi.org/10.1016/j.corsci.2019.04.005

Smart-release inhibition of corrosion driven organic coating failure on zinc by cationic benzotriazole based pigments

C.A.J. Richards*, H.N. McMurray, G. Williams

Materials Research Centre, College of Engineering, Swansea University, Bay Campus, Fabian Way, Swansea, UK, SA1 8EN.

*Corresponding author: Tel: 07889271936, E-mail address: 557333@swansea.ac.uk

Highlights

- A benzotriazole derived pigment system is shown to inhibit cathodic delamination on zinc.
- The system demonstrates an inhibition efficiency approaching that of strontium chromate.
- Inhibition of cathodic oxygen reduction reactions by benzotriazole is proven.

Abstract

A novel cationic benzotriazole pigment (CBP) based on the benzotriazolium cation ($BTAH_2^+$) exchanged into a sulfonated organic resin has been synthesized and evaluated as a means of inhibiting the corrosion-driven cathodic disbondment of organic coatings from the surface of galvanized steel. The CBP is acidic in nature ($BTAH_2^+$ $pK_a \approx 1.1$) and is intended to be compatible with acidic coating formulations such as etch-primers. Delamination rates, as measured using a scanning Kelvin probe (SKP), were found to decrease monotonically with increasing CBP volume fraction (Φ_{CBP}) and to approach zero when $\Phi_{CBP} = 0.1$. The mechanism of CBP operation is described.

Keywords: benzotriazole, corrosion, inhibition, zinc, galvanized steel.

1. Introduction

Organically coated galvanized steel (OCS) is a multi-billion-pound industry and represents a significant portion of the finished-steel market [1]. Favoured for the on-demand and bespoke supply chains, products currently offer robust lifetime guarantees - upwards of 30 years [1]. These guarantees are largely afforded by the corrosion inhibiting properties of hexavalent chromium and its chromate derivatives in the form of soluble salts such as strontium and zinc chromate dispersed as pigments within a protective organic coating. Despite their currently unmatched corrosion inhibiting potency, these compounds are extreme health hazards and are classed as genotoxic carcinogens [2-5].

Recent research has been focused on finding suitable alternatives that can match chromates in their ability to inhibit the corrosion mechanisms that lead to the failure of OCS products without the associated hazards. Within the literature, there have been numerous candidate replacement chemistries, including: zinc salts, phosphates and rare earth species. However, alternatives have struggled to match the performance of chromate systems [6-9].

The high efficiency of chromate-based pigments as corrosion inhibitors for organically coated metal surfaces is thought to result from their particular mechanism of operation. For example, in the case of strontium chromate ($SrCrO_4$) pigments it has been shown that CrO_4^{2-} anions diffusing beneath an organic coating can effectively inhibit cathodic disbondment [6, 10-13]. This mode of inhibition has been ascribed to CrO_4^{2-} reduction replacing oxygen reduction in the cathodic reaction, the product being an insoluble, electrically insulating $Cr(OH)_3$ precipitate. This process is self-limiting and effectively stifles further O_2 reduction. However, for ferrous alloys (and possibly some non-ferrous) it has been argued that chromate can provide anodic inhibition by acting as a ‘passivator’, that is an oxidizing agent which increases the open circuit potential of the alloy, passivating the surface.

The typical makeup of an OCS product consists of an initial pre-treatment coating, also known as a conversion coating, which is effectively a wash that prepares the metallic surface and provides better adhesion to the subsequent primer coating. The primer coating contains the bulk of the corrosion inhibitor, it then receives a topcoat which acts as a barrier to the outer environment and determines the overall appearance and aesthetics of the product [1]. Current chrome-free primer formulations that provide acceptable corrosion protection remain reliant on chromate-based pre-treatments [6,14]. However, an alternative approach involves the use of a "pre-treatment primer" systems, sometimes referred to as "etch-primers", these avoid the use of a separate pre-treatment step in coating preparation. A typical etch primer formulation would comprise of a film forming polymer, such as polyester or polyurethane, and phosphoric acid (H_3PO_4), dissolved in a suitable solvent, such as butanone [14,15].

Various inorganic and organic corrosion inhibitors have been proposed as potential chromate replacements, either alone or in combination [6-9]. Furthermore, a number of "smart-release" strategies have been described which allow these inhibitors to be converted into coating-compatible pigments capable of releasing the inhibitor species as and when required [16-19]. Benzotriazole is a heterocyclic aromatic organic compound known for its versatility and application in many fields, in particular, as a corrosion inhibitor for copper (and associated alloys) in both atmospheric and submerged conditions [20,21]. Other works have also demonstrated benzotriazole as an effective inhibitor to the corrosion of aluminium and zinc [22,23]. The benzotriazole anion (benzotriazolate (BTA^-)) has been exchanged into hydrotalcite (a layered double hydroxide (LDH)) to produce corrosion inhibitor pigments suitable for dispersion in organic coatings applied to metallic substrates [24-26]. The greater part of work published on such BTA^-/LDH pigments relates to the protection of aluminium alloys. However, benzotriazole has also been studied as an inhibitor for organic coated zinc or galvanized steel. For example, benzotriazole has been incorporated into mesoporous SiO_2

layers applied to galvanized steel [27]. benzotriazole has also been used to impregnate polymeric core-shell nanocontainers based on poly-acrylic acids and incorporated into organic coatings for the protection of galvanized steel [28]. Anti-corrosion pigments have also been developed based on sparingly soluble zinc-BTA complexes [29].

Benzotriazole is an amphoteric compound and can therefore exist in neutral, anionic and cationic forms, depending on solution pH. [20]. The protonic equilibria linking the various benzotriazole species, together with the relevant pK_a values, are shown in equations (1) and (2) [20] and Fig. 1 shows the relative concentrations of the various species as a function of pH.

$$BTAH_2^+ \leftrightarrow BTAH + H^+ \qquad pK_1 \approx 1.1 \qquad (1)$$

$$BTAH \leftrightarrow BTA^- + H^+ \qquad pK_2 = 8.2 \qquad (2)$$

Figure 1

Fagel and Ewing et al [30] demonstrated that the UV absorption of benzotriazole in aqueous solution is strongly pH dependant. A single absorption peak (λ_{max} = 274 nm) is observed for strongly acidic conditions (pH < 0) where the $BTAH_2^+$ cation predominates. A single peak (λ_{max} again 274 nm) is also observed under strongly basic conditions (pH > 10) where the BTA^- anion predominates. Two absorbance peaks (λ_{max} = 274 nm and 260 nm) are observed at intermediate values of pH where neutral benzotriazole predominates. The $BTAH_2^+$ cation is predicted to be stable in the presence of strongly acidic species such as those found in etch primer formulations.

In this paper, we present a systematic study aimed at characterising a novel $BTAH_2^+$ cation exchanged corrosion-inhibitor pigment prepared by reacting neutral benzotriazole with a crosslinked polystyrene sulfonic acid resin (Amberlite 120 H^+). The formation reaction relies on the sulfonic acid functional groups of the resin (pK_a -2.8) being significantly more acidic

than the pK_a of 1.1 associated with reaction (1) so that the resulting proton transfer produces $BTAH_2^+$ in situ., as shown schematically in Fig. 2a. In principle, the $BTAH_2^+$ cation can be released through an exchange equilibrium with cations present in an aqueous electrolyte at any pH. However, at the alkaline pH prevailing at sites of local net cathodic activity any $BTAH_2^+$ so released will become rapidly deprotonated, as shown schematically in Fig. 2b. Under these circumstance the exchange equilibrium will be continually displaced in favour of further $BTAH_2^+$ release, so that the release process is predicted to become particular efficient. Here we follow the kinetics associated with the reaction schemes in Fig. 2a and Fig. 2b spectrophotometrically.

Figure 2

The cationic benzotriazole pigment (CBP), produced as below, is evaluated as a corrosion inhibitor by dispersion in an ethanolic solution of polyvinyl butyral (PVB) which is then coated onto the cleaned surface of hot dip galvanised (HDG) steel coupons. Using a "Stratmann type" experiment [31-33], a penetrative organic coating defect is formed, and a corrosive (aqueous sodium chloride) electrolyte introduced. The resulting corrosion-driven cathodic coating disbondment is followed using a scanning Kelvin probe (SKP) instrument. By this means the effect of varying the CBP volume fraction (Φ_{CBP}) in the organic coating is systematically determined. To help explain the mode(s) of operation by which benzotriazole inhibits corrosion-driven coating failure, the inhibition of cathodic oxygen reduction, reactions (3) and (4), on zinc (HDG steel) by BTA^- dissolved in an aqueous electrolyte is investigated using potentiodynamic polarization in combination with a rotating disk electrode (RDE) apparatus, which ensures reproducible conditions of mass transport for electroactive species (in this case O_2).

4*e*⁻ $O_2 + 2H_2O + 4e^- \rightarrow 4OH^-$ (3)

2*e*⁻ $O_2 + H_2O + 2e^- \rightarrow HO_2^- + OH^-$ (4)

2. Materials and Methods

Materials: HDG steel coupons of 0.7 mm gauge mild steel coated on both sides with a 20 μm zinc layer (containing 0.15% aluminium) were supplied by Tata Steel UK. These were subsequently cut into 5 cm square coupons and used as substrates in the programme of experimental work. The as received material had been produced by skin passing and tension levelling following hot-dip galvanization. Zinc samples of 99.9% purity were purchased from Goodfellow Ltd. Benzotriazole, polyvinyl butyral, Amberlite® 120 H^+ and all other chemicals were purchased from the Sigma-Aldrich Chemical Co. and were of analytical grade purity. Hellma 10 mm 100 QS (3.5×10^{-3} L) quartz cuvettes were also purchased from the Sigma-Aldrich Chemical Co.

Methods

Spectrophotometric determination of benzotriazole: All optical absorbance measurements were performed at pH 11 using a PerkinElmer Lambda 750 UV/VIS/NIR Spectrometer in conjunction with a 1 cm quartz cuvette. A calibration curve was prepared by plotting the absorbance measured at λ_{max} = 274 nm as a function of BTA^- concentration between 1×10^{-5} and 1×10^{-4} M. The resulting plot was a good straight line ($R^2 = 0.9988$) implying that at pH 11 aqueous [BTA^-] (between concentrations of 1×10^{-5} and 1×10^{-4} M) obeys the Beer-Lambert law, equation (5), and that significant association, precipitation or surface absorption of BTA^- anions do not occur over the stated concentration range.

$$A_{274} = \varepsilon_{274}\, c\, l \quad (5)$$

where ε_{274} is the molar extinction coefficient at 274 nm, c is concentration in M and l is the optical path length in cm. The value of ε_{274} obtained from the least-squares analysis of absorbance data was 9700 M^{-1} cm^{-1} (+/- 200) at ~20°C. Thereafter, the solution concentration of benzotriazole species (at any pH) was determined by withdrawing an aliquot, volumetrically diluting with distilled water (if necessary), adjusting the pH to 11 with aqueous NaOH and measuring the optical absorbance at 274 nm.

Preparation of $BTAH_2^+$ exchanged resin: The quoted volume exchange capacity of Amberlite 120 H^+ is 1.8 eq L^{-1} [34] and the density is 1.2 kg L^{-1}. On this basis, the exchange capacity of the resin, per-weight, may be calculated as 1.5 milliequivalents (mEq) per gram. The molecular weight of the benzotriazole is 119.13 g mol^{-1} implying that, when fully exchanged, 100 g of resin should hold 17.87 g of $BTAH_2^+$. From these estimates, an excess of benzotriazole was calculated to ensure resin saturation. Thus, 0.2 M (23.82 g) of benzotriazole was dispersed in 1 L solution of distilled water. The dispersion was heated to 60°C, at which temperature benzotriazole readily dissolves as neutral benzotriazole, and 100 g of Amberlite 120 H^+ beads added. This mixture was then stirred at a constant speed for 2 hours using a magnetic stirrer.

The process of benzotriazole uptake was followed by periodically drawing small (0.1 ml) aliquots of the hot benzotriazole solution from the reaction mixture using a micropipette over a 2-hour period. Fig. 3 shows the concentration of neutral benzotriazole in contact with Amberlite 120 H^+ as a function of time (for 100 ml of solution and 10 g of resin) falls by approximately 72.5% from 0.2 M to 0.055 M and becomes approximately constant after 30 minutes. These findings imply that, at equilibrium, the $BTAH_2^+$ exchange capacity of the Amberlite 120 H^+ resin may be calculated as 1.59 mEq g^{-1}, which is in good agreement with

the value of 1.5 mEq / 100 g derived from the manufacturers' specification. Furthermore, the $BTAH_2^+$ uptake kinetics are relatively fast, reaching 90% completion in ~10 minutes.

Figure 3

At the end of the 2-hour exchange period the resin beads were collected using a Buchner filtration system, washed with 500 ml of deionised water, and then dried for 24 hrs at 40°C under vacuum. Once dried, the exchanged Amberlite 120 H^+ resin beads were milled using a Retsch planetary ball mill at 350 RPM for 2 hours. The resulting powder was then sieved through a 20 μm mesh, yielding a finely divided cationic benzotriazole pigment, hereafter referred to as CBP.

Rotating disk electrode polarization measurement: For RDE measurements of O_2 reduction kinetics on zinc, disks of HDG steel (18 mm diameter) were used as the working cathode. The HDG zinc surface was prepared by lightly abrading with silicon carbide paper (1200 μm grit) and polishing with an aqueous slurry of 5 μm alumina followed by acetone rinse and air drying. All electrochemical measurements were performed in aerated conditions at 20°C in 0.5 M aqueous sodium sulfate electrolyte, containing 0.05 M sodium tetraborate ($Na_2B_4O_7.10H_2O$) and 0.1 M sodium hydroxide (NaOH), which gave a buffered pH of 9.3. When required, benzotriazole was added to the experimental electrolyte at concentrations of 2×10^{-2}, 2×10^{-3}, 2×10^{-4} or 2×10^{-5} M, with further additions of sodium hydroxide made in order to maintain a pH of 9.3. At the experimental pH, zinc is not active (i.e. zinc oxidation products are insoluble), thus avoiding high zinc dissolution rates [35]. Samples were mounted in the PTFE holder of an Oxford Instruments RDE-2 rotating disk electrode system supplied by Sycopel Scientific. A Gamry mercury/mercurous sulfate reference electrode and a platinum gauze counter electrode were used in a standard 3 electrode cell arrangement. Polarization of the working

electrode was carried out using a Solartron 1280 potentiostat. Prior to each experiment, the working electrode was held at a potential just above the onset of visible hydrogen evolution for two minutes in order to reduce any air-formed oxide film. Quasi-steady state polarization curves were obtained using linear potential sweep rate of 3.3×10^{-4} V s^{-1} and a rotation head speed of 217 rad s^{-1} following a methodology described elsewhere [36-38].

Benzotrialzole release kinetics from cationic-exchange resin: The release kinetics of benzotriazole species from the fully [$BTAH_2^+$] exchanged Amberlite 120 H^+ resin were determined using 1 M aqueous NaOH as a model for the alkaline electrolyte forming at sites of local cathodic activity. A 10 g quantity of [$BTAH_2^+$] exchanged resin beads (prepared as before) were stirred in 100 ml of 1 M aqueous NaOH for twenty minutes at room temperature. Aliquots of solution (0.1 ml) were withdrawn periodically, diluted to 100 ml with distilled water and adjusted to pH 11 using aqueous NaOH. This procedure was repeated three times, until ~96% of the $BTAH_2^+$ originally present in the resin had been released.

Corrosion driven cathodic delamination measurements: The HDG zinc surface was prepared for coating using an aqueous slurry of 5 µm alumina to remove the as-received surface including any contaminants and/or pre-existing oxide layer. Degreasing was carried out via an acetone rinse followed by air-drying. PVB solutions MW 70,000-100,000 were prepared in ethanol (15.5% w/w), the required amounts of CBP were added and thoroughly mixed using a shear mixer. Organic coatings (films) were produced by bar casting the PVB/CBP dispersion onto the relevant substrate using electrical tape (~145 µm in thickness) as a height guide. This resulted in a dry film thickness of ~16 µm (measured by a micrometre screw gauge). The volume fraction (Φ_{CBP}) of the CBP in the PVB dispersions was calculated using:

$$\Phi_{CBP} = \left(1 + \frac{M_{PVB} \cdot \rho_{Pig.}}{M_{pig} \cdot \rho_{PVB}}\right)^{-1} \quad (6)$$

where M_{PVB} is the mass of PVB used in the coating formulation, M_{pig} the mass of CBP, ρ_{PVB} the density of PVB (~0.8 g cm^{-3}) [41] and ρ_{pig} is the density of Amberlite 120 H^+ (~1.8 g cm^{-3}) [34]. Strong PVB film adhesion to the HDG substrate was observed and it was not possible for the films to be peeled off by hand.

The delamination sample cell preparation procedure was based on the methods presented by Stratmann et al [31, 39, 40]. All corrosion-driven cathodic delamination experiments were carried out in an enclosed SKP chamber containing air and maintained at a constant 96% R.H. and 20˚C. Delamination was initiated by introducing ~2 cm^3 of 0.86 M aqueous NaCl electrolyte at pH 7 into the penetrative coating defect (area ~1 cm by 2 cm rectangle). The SKP reference probe consisted of a gold wire of diameter 125 µm vibrating vertically at 280 Hz and amplitude of 40 µm at a distance of 100 µm above the sample surface. E_{corr} data points were recorded at a density of 20 points per mm. The SKP reference probe was scanned over the coated surface along a 12 mm line normal to, and adjacent with, the defect-coating boundary. Scanning commenced immediately on the addition of electrolyte and thereafter at hourly intervals over a period of ≥ 24h.

Design and operation of the SKP apparatus has been described extensively elsewhere [31, 39, 40], including the procedure for calibrating the SKP in terms of local free corrosion potential (E_{corr}). Following this calibration procedure, it was shown that for a metal surface covered with an adherent PVB film, or with a PVB film which has become delaminated through the ingress of a thin electrolyte film, that

$$E_{corr} = \Delta\Psi_{Pol}^{Ref} + C \ \text{V vs. SHE} \quad (7)$$

where $\Delta\Psi_{Pol}^{Ref}$ is the Volta potential difference measured between the SKP reference probe and the polymer/air interface and calibration constant (*C*) determined by placing a free standing PVB film over a calibration cell, as described elsewhere [31,39,40]. Where no defect region is present (i.e. no progression of the delamination front) the adherent intact coating region is referred to as E_{intact}. A schematic representation showing the movement of the SKP probe relative to the experimental sample and the relationship between the cathodic delamination cell and the potential profile recorded by SKP is given in Fig. 4.

Figure 4

3. Results and Discussion

Inhibition of cathodic delamination by CBP: Prior to the introduction of corrosive electrolyte (0.86 M NaCl) at the coating defect the potential (E_{intact}) measured over the intact PVB coated zinc surface at 96% RH was recorded over a 20 hour period. Fig. 5 shows area-averaged E_{intact} values plotted as a function of time for PVB coatings with Φ_{CBP} = 0, 0.01, 0.025, 0.05 and 0.1. In all cases E_{intact} increases gradually over time, becoming approximately constant (time-independent) after approximately 10 hours. The time-independent (final) values of E_{intact} progressively decrease with increasing Φ_{CBP} and when Φ_{CBP} = 0.1 the time-independent E_{intact} is approximately 0.1 V lower that in the case of unpigmented PVB.

Figure 5

The significance of E_{intact} for polymer-coated metal has been discussed at length elsewhere. Briefly, for nonconducting polymers, E_{intact} reflects the open-circuit potential of the oxide-covered metal surface, influenced as this may be by reactions with atmospheric O_2 and/or Bronsted acid-base interactions occurring between the oxide and polymer coating [10, 32, 42]. On this basis the time-dependent evolution of E_{intact} values in Fig. 5 most probably reflects the time taken for (electro)chemical reactions occurring at the coating-zinc interface to reach a

steady-state. Furthermore, mixed potential theory would suggest that the slight depression of time-independent E_{intact} values with increasing Φ_{CBP} is consistent with the CBP pigment acting to inhibit cathodic processes and/or facilitate anodic processes occurring at the coating-zinc interface.

When corrosive electrolyte was introduced into the defect in unpigmented PVB coatings delamination was found to become initiated within 2 hours of electrolyte contact. Thereafter, time-dependent E_{corr} *vs*. distance (x) from the defect edge profiles became established as shown in Fig. 6 a). In the intact coating region potentials (E_{intact}) are relatively high because anodic zinc dissolution is disfavoured in the absence of liquid electrolyte. Conversely, in the near-defect region potentials (E_{corr}) fall to values expected for freely corroding zinc, shown schematically in Fig. 4. Ionic current flux passing along the thin layer of electrolyte which ingresses beneath the delaminated coating produces in an ohmic potential gradient linking the net anode at the coating defect to the site of cathodic oxygen reduction, reactions (3) and (4), at the coating delamination front. Current in the underfilm electrolyte is carried by Na^+ ions migrating from the external electrolyte to balance the charge of OH^- produced through reaction (3). External electrolyte anions (in this case Cl^-) are migrationally excluded. The the under-film electrolyte becomes alkaline (pH > 10) due to the formation of sodium hydroxide [33].

Figure 6

The time-dependent $E_{corr(x)}$ profiles were found to become significantly modified when the coatings contained CBP. Fig. 6 b) shows representative $E_{corr(x)}$ profiles obtained from a pigmented PVB coating containing $\Phi_{CBP} = 0.01$. A comparison of Figs. 6 a) and b) shows that the extent of delamination occurring after a holding period of 24 h is significantly reduced (relative to unpigmented PVB) when the CBP is present. Furthermore, values of E_{corr} measured in the near-defect region are ~0.1V higher for the $\Phi_{CBP} = 0.01$ case than for the unpigmented

coating. Systematically increasing Φ_{CBP} was found to produce a progressive reduction in the rate of delamination and when $\Phi_{CBP} \geq 0.1$ no indication of coating delamination was observable over the 24-hour experimental period, as shown in Fig. 6 c).

The rate (lateral velocity) of cathodic delamination may be quantified by taking the position of the delamination front to be point of maximum potential gradient in successive time-dependent E_{corrx} profiles [31-33]. Delamination kinetics may then be determined by plotting the delaminated distance (x_{del}) against (t_{del} - t_i), where t_{del} is the time since electrolyte introduction and t_i is the time taken for delamination to become initiated. Fig. 7 shows a series of (x_{del}) *vs.* (t_{del} - t_i) curves thus obtained for: unpigmented PVB and various values of Φ_{CBP} up to Φ_{CBP} = 0.1. It may be seen that increasing Φ_{CBP} produces a significant reduction in delamination rate but also a change in kinetic order with respect to time, from parabolic ($t^{1/2}$ dependence) to zero order (linear with respect to t).

Figure 7

Parabolic delamination kinetics are frequently observed in the case of uninhibited coatings [10, 31-33, 39, 40] and are typically the result of underfilm cation migration (here Na^+) being the rate determining process [32, 33]. The change to linear kinetics observed in the presence of CBP is consistent with a vertical process (one not dependent on x_{del}) becoming rate determining as Φ_{CBP} increases. Such a vertical process could be either: i) diffusional mass transport of O_2 through the coating [43] or ii) the electrochemical electron transfer process associated with the cathodic oxygen reduction reaction (3). Since the transition to linear kinetics is observed when Φ_{CBP} is as low as 0.01 (under which circumstance it is very unlikely to significantly affect O_2 transport) the most probable cause is an inhibition of underfilm cathodic O_2 reduction.

Because of the change from parabolic to linear kinetics, shown in Fig 7, the initial rate of coating delamination was used as a means of making a comparison between unpigmented PVB

and the various coatings containing different Φ_{CBP}. In each case, the initial delamination rate was obtained by determining the gradient (dx_{del}/dt) of a tangent constructed to the relevant (x_{del}) *vs.* (t_{del} - t_i) curve at (t_{del} - t_i) = zero. Fig. 8 shows normalised values of initial delamination rate plotted of as a function of Φ_{CBP}. In order to better assess the likely usefulness of CBP as an inhibitor of cathodic disbondment on zinc Fig. 8 also shows normalized data obtained from a previously published study of inhibition by a strontium chromate pigment [10]. Comparison of the CBP and strontium chromate derived data in Fig. 8 shows that for pigment volume fraction (Φ) values < 0.5 CBP actually seems more efficient than strontium chromate. However, it should also be noted that strontium chromate produces immeasurably slow delamination at Φ = 0.08, whereas for CBP the same occurs when Φ = 0.1. It should also be borne in mind that the experiments described here pertain only to cathodic disbondment and not the full range of corrosion phenomena that can affect an organic coated metal.

Figure 8

Possible modes of CBP-substrate interaction: Three modes of CBP-substrate interaction may be thought of as possibly contributing to the inhibition of corrosion-driven cathodic disbondment described above. These are as follows

1. Modification of the zinc surface through reaction with CBP prior to the addition of the corrosive electrolyte.
2. Inhibition of underfilm cathodic O_2 reduction as a result of benzotriazole being released into the underfilm electrolyte.
3. Inhibition of anodic zinc dissolution at the coating defect site as a result of benzotriazole species being released into the defect (external) electrolyte.

Mode 3 is not expected make a significant contribution to the overall inhibition of cathodic disbondment in the experiments described here for the following reasons:

a) No visible change in corrosion at the defect site was observed with increasing CBP, in all cases the zinc surface exposed at the defect became heavily corroded.
b) Relatively low concentrations of benzotriazole species will be produced in the (2 cm^3) volume of defect electrolyte.
c) The defect area is large (1 cm^2), requiring a very profound inhibition to occur if anodic current contributions tend to become rate determining.

It would therefore seem likely that the greater part of an observed inhibition results from a combination of Modes 1 and 2.

In consideration of mode 1, it should be noted that the acidic $BTAH_2^+$ cations exchanged into the CBP could, in principle, undergo deprotonation in the presence of zinc and zinc (hydr)oxide species via reactions (8-10).

$$Zn + 2BTAH_2^+ \rightarrow Zn^{2+} + H_2 + 2BTAH \quad (8)$$

$$Zn(OH)_2 + 2BTAH_2^+ \rightarrow Zn^{2+} + 2H_2O + 2BTAH \quad (9)$$

$$Zn(OH)_2 + 2BTAH \rightarrow Zn(BTA^-)_2 + 2H_2O \text{ , } pK_a \sim 8.2 \quad (10)$$

Reactions (8) and (9) both have cationic products (Zn^{2+}) which would allow further $BTAH_2^+$ to be released from the CBP via a cation exchange process. The Φ_{CBP} dependent changes in E_{intact} shown in Fig. 5 are consistent with some degree of reaction occurring between the (oxide covered) zinc surface and CBP prior to introduction of the corrosive electrolyte. However, because this involves an essentially solid-solid reaction mechanism, which can only occur at points of contact between CBP particles and the zinc substrate, it is likely that mode 1 is

relatively inefficient and only a small fraction of the $BTAH_2^+$ initially present in the CBP is capable of reacting in this way.

In consideration of mode 2, a question arises as to what fraction of the $BTAH_2^+$ cations exchanged into the CBP is capable of being released into the alkaline electrolyte film forming beneath the delaminated coating and how quickly that release can occur. In order to better determine these quantities inhibitor release experiments were performed using an excess of 1 M aqueous NaOH as model for the alkaline underfilm electrolyte, as detailed in the experimental section. A large excess of NaOH was employed to ensure that the availability of base did not limit the extent or rate of inhibitor release. Amberlite resin beads exchanged with $BTAH_2^+$ were used in these experiments, rather than the CBP power produced by grinding the beads, because of the difficultly in handling aqueous dispersions of CBP. Consequently, the measured rates of inhibitor release probably underestimate the rates achievable from the CBP itself.

The proposed release mechanism is shown schematically in Fig. 2b, whereby $BTAH_2^+$ cations in the resin exchange with the Na^+ ions in solution and subsequently undergo a rapid coupled homogenous deprotonation through reaction with aqueous hydroxide, yielding BTA^- anions. Fig. 9 shows the concentration of released BTA^- plotted as a function of time for three successive release experiments in which the same 10 g of $BTAH_2^+$ exchanged beads were stirred with fresh 100 ml aliquots of 1 M aqueous NaOH for 20 minutes at room temperature. From the data in Fig. 9 it is possible to calculate that approximately 80% of the available BTA^- is released by the end of the first release experiment, 90% by the end of the second, and 96% at the end of the third. A comparison of Figs. 3 and 9 indicates that the kinetics of BTA^- release at room temperature are somewhat slower that the kinetics of benzotriazole uptake at 60°C. Nevertheless, BTA^- release is sufficiently rapid and complete as to suggest that useful amounts

will be release into the underfilm catholyte over the timescale of a typical cathodic disbondment experiment.

Figure 9

Inhibition of electrochemical kinetics by benzotriazole: Given the arguments developed in the preceding sections, a question arises as to what extent benzotriazole species released from the CBP pigment are capable of inhibiting electron transfer processes, particularly those associated with reactions (3) and (4). To this end a series of potentiodynamic polarization experiments were carried out to quantify the effect of varying electrolyte BTA^- anion concentrations ($[BTA^-]$) on the kinetics of the cathodic oxygen reduction reaction (CORR) as it occurs at the HDG steel zinc surface. In so doing a rotating disk electrode (RDE) apparatus was used to ensure reproducible conditions of mass transport for electroactive species (in this case O_2). The electrolyte conditions, 0.5 M aqueous sodium sulfate buffered to pH 9.3 with borate buffer, were selected to minimize rates of zinc dissolution and maximize comparability with previously published work [36-38]. To an extent these conditions represent a reasonable model for a mildly alkaline underfilm electrolyte. However, they differ in one important respect, the underfilm electrolyte will contain no aggressive anions (sulfate or chloride) derived from the external electrolyte [33].

Cathodic-going scans starting from the open circuit potential (OCP) were used to ensure that the zinc surface was in a state that resembled (as near as possible) the free corrosion condition. A slow potential scan rate (3.3×10^{-4} V s^{-1}) was used to produce a quasi-potentiostatic measurement, in which the current densities measured were close to being steady-state values. Fig. 10 shows cathodic polarization curves obtained for the HDG zinc surface under aerated conditions using an RDE rotation angular velocity of 217 rad s^{-1}. At the experimental pH (9.3)

benzotriazole (pK_a = 8.3) will be predominantly (~90%) deprotonated via reaction (2) to anionic BTA^-. The electrolyte BTA^- concentration, for the various curves in Fig. 10 are a) zero, b) 2×10^{-5} M, c) 2×10^{-4} M, d) 2×10^{-3} M and e) 2×10^{-2} M, respectively. Curve a) is basically similar to data reported previously for zinc cathodically polarized in aerated aqueous chloride electrolyte [37]. The current plateau (~1.5 mA cm^{-2}) seen between (approximately) -1.04 V and -1.15 V corresponds to a diffusion limited 4 electron reduction of O_2, reaction (3) occurring on bare metallic zinc. At potentials > -1.04 V the zinc surface becomes covered with a zinc (hydr)oxide film and 2 electron O_2 reduction, reaction (4), is expected to predominate. [36].

The potential dependence of cathodic currents in the region of curve a) lying between -1.04 V and the open circuit potential (OCP) of ~0.85 V suggests that over this potential range reaction (4) is occurring substantially under activation (electron transfer) control.

Figure 10

A comparison of the various polarization curves in Fig. 10 indicates that as [BTA^-] increases, cathodic current densities are significantly reduced relative to the uninhibited case. This effect is most fully demonstrated in curves d) and e), which show no evidence of any diffusion-limited current plateau. Furthermore, over the potential range -0.85 V to -1.05 V, where reaction (4) is expected to dominate, current densities in curves d) and e) are reduced by up to 90% compared to curve a). The polarization curves in Fig. 10 can be further analysed to determine values of OCP and polarization resistance (R_p). The latter is calculated as the reciprocal gradient of a tangent constructed to the curve at OCP (i = zero). Fig. 11 shows OCP and R_p values thus obtained plotted as a function of [BTA^-].

Figure 11

It may be seen from Fig. 11 that OCP increases monotonically with increasing [BTA^-]. This finding implies that is actually acting as a mixed (anodic and cathodic) corrosion inhibitor, as

has been reported elsewhere [44]. It further implied that, that although Fig. 10 indicates that BTA^- it is an effective inhibitor of the CORR, it is its action an anodic inhibitor which predominates under free corrosion conditions. Fig. 11 shows that R_p also increases with increasing $[BTA^-]$ for all $[BTA^-] \leq 2 \times 10^{-3}$ M but decreases again slightly when $[BTA^-]$ is increased to 2×10^{-2} M. The various values of R_p may be used to estimate the effect of varying $[BTA^-]$ on the corrosion current density (i_{corr}) using the Stern-Geary relationship, equation (11).

$$R_p = \frac{B}{i_{corr}} \qquad (11)$$

where i_{corr} is the corrosion current and B is given by

$$B = \frac{b_c \cdot b_a}{2 \cdot 3(b_a + b_c)} \qquad (12)$$

where b_a and b_c are the anodic and cathodic Tafel slopes respectively. From equations (11) and (12) it is evident that R_p will be inversely proportional to the free corrosion current provided b_a and b_c are assumed to be constant. On this basis, the data in Fig. 11 implies that corrosion inhibition by BTA^- reaches a maximum efficiency of ~90% at (or near) $[BTA^-] = 2 \times 10^{-3}$ M under free corrosion conditions. The reason for inhibition efficiency decreasing slightly when $[BTA^-]$ is increased to 2×10^{-2} M remains unclear.

The findings outlined above have a number of implications:

1) BTA^- is an effective inhibitor of the CORR on zinc under mildly alkaline conditions and this is consistent with the notion that the CBP inhibits cathodic coating disbondment by inhibiting underfilm CORR.

2) In terms of the inhibition of cathodic disbondment the maximum efficiency exhibited by the CBP (~100% at Φ_{CBP} =0.1) is significantly greater that the maximum efficiency predicted from the R_p values in Fig. 11 (~90% at $[BTA^-] = 2 \times 10^{-3}$ M). This difference is presumably the

consequence of aggressive anions (Cl^- or sulfate) being excluded from the underfilm electrolyte layer and also the possibility of underfilm pH becoming > 9.3.

3) The finding that BTA^- is a mixed inhibitor with a tendency to increase OCP (predominantly anodic inhibition) is consistent with the increase in near-defect E_{corr} values observed when coatings contain CBP, as in Fig. 6.

The Mechanism of benzotriazole Inhibition: As previously stated, benzotriazole has a long history in the field of corrosion, where it has predominantly been used as an inhibitor for the protection of copper and brasses. However, uncertainty still persists in explaining the exact mechanisms by which benzotriazole affords inhibition [20, 21, 45]. This uncertainty arises from the varying phenomena that interplay at the metal surface under corrosion conditions. For transition metals (Fe, Cu and Zn) two principal mechanisms have been proposed, the first attributes inhibition to adsorption of benzotriazole species at the metal surface via reaction (13) [46-50]

$$[BTAH]_{aq} + M_{(s)} \rightarrow [BTAH]_{ads} : M \qquad (13)$$

where $M_{(s)}$ represents a transition metal surface atom. The second mechanism is characterised by the precipitation of a metal-BTA complex that forms a densely packed polymeric film following reactions (14) and (15) [45, 46, 50, 51]

$$M_{(s)} + BTAH \rightarrow MBTA + H^+ + e^- \quad pK_a \sim 8.2\ BTAH \qquad (14)$$

$$n(MBTA) \rightarrow (MBTA)_n \qquad (15)$$

where reaction (14) shows the complex formation and reaction (15) the development of a polymeric structure. It has also been suggested that the adsorption and complex formation reactions described here are in equilibrium [52, 53]

$$nBTAH_{ads} + nM \leftrightharpoons (MBTA)_n + nH^+ + ne^- \qquad (16)$$

This implies that the at higher pH values, the polymeric film complex is favoured, whereas at lower pH, adsorption becomes more favourable. The underfilm electrolyte of a cathodic disbondment cell exhibits a high pH, in the case of zinc it can reach pH 11 [33]. Therefore, it would be expected that reaction (14) would dominate in the underfilm environment associated with cathodic disbondment. Furthermore, it has been demonstrated that benzotriazole can produce dense films on zinc under alkaline conditions [45, 46, 50-53]. It therefore seems reasonable to propose that the inhibition of corrosion-driven organic coating disbondment by CBP is consistent with the formation of a BTA-derived polymeric film complex at the under-film zinc surface.

4. Conclusion

A novel corrosion inhibitor pigment (CBP) based on the benzotriazolium cation ($BTAH_2^+$) exchanged into a sulfonated organic resin (Amberlite 120 H^+) has been synthesized and evaluated as a means of slowing the corrosion-driven cathodic disbondment of organic coatings from the surface of galvanized steel (HDG). The CBP is acidic in nature ($BTAH^{2+}$ $pK_a \approx 1.1$) and is therefore likely to the compatible with acidic coating formulations such as etch-primers and/or pre-treatment primers containing acids such as phosphoric acid, tetravalent titanium species or tetravalent zirconium species. The $BTAH_2^+$exchange capacity of the resin was found to be 1.59 mEq / 100 g and ~80% of this capacity becomes released (and converted to the benzotriazolium anion (BTA^-) within 20 minutes of contact with 1 M aqueous alkali.

The BTA^- anion thus released has been investigated as an inhibitor of cathodic O_2 reduction reactions (CORR) and anodic zinc dissolution by using potentiodynamic polarization measurements in combination with a rotating disk electrode. Under near neutral (9.3 pH)

conditions in air saturated aqueous sodium sulfate solution. BTA^- was found to be a mixed (anodic and cathodic) inhibitor with an inhibition efficiency of up to 90% (at a [BTA^-] concentration of 2×10^{-3} M), calculated on the basis of changes in polarization resistance at the open circuit potential (OCP). The CORR were profoundly inhibited on the zinc surface of HDG but inhibition of anodic zinc dissolution was the predominant effect, as evidenced by a monotonic increase in OCP with increasing BTA^- concentration.

Quantities of CBP dispersed in an organic coating (PVB) applied to the zinc surface of HDG were found to inhibit the kinetics of corrosion-driven cathodic delamination, as produced when aqueous sodium chloride solution was brought into contact with a penetrative coating defect. Delamination rates, as measured using a scanning Kelvin probe (SKP), were found to progressively decrease with increasing CBP volume fraction (Φ_{CBP}). Furthermore, when Φ_{CBP} was increased to 0.1 delamination rates became immeasurably slow, implying an inhibition efficiency significantly greater than the 90% measured in aqueous sodium sulfate. On the basis of these findings it is proposed that the CBP pigment acts to produce a rapid and efficient release of BTA^- species into the alkaline catholyte film forming beneath the delaminating coating. It is further proposed that the high pH of this catholyte coupled with the absence of aggressive anions (anions from the external electrolyte will be migrationally excluded) facilitate the formation of a BTA^- derived film at the zinc surface which efficiently inhibits the under-film CORR.

5. Acknowledgements

The authors recognise the EPSRC, Welsh Government and Tata Steel UK for financial support of this work and Innovate UK for the SPECIFIC Innovation and Knowledge Centre (grant numbers EP/I019278/1, EP/K000292/1, EP/L010372/1)

References

[1] Jörg Sander. 1.0 Coil Coating – principle, market and applications. In: Coil Coating, Vincentz, Hanover, Germany 2014
[2] U.S. Environmental Protection Agency, Health Assessment Document for Chromium, Final Report, EPA-600/8-83-014F
[3] S. A. Katz and H. Salem, The toxicology of chromium with respect to its chemical speciation: a review. J. Appl. Toxicol., 13, (1993) pp. 217
[4] S. Langard and T. Norseth, Occurrence of lung cancer in workers producing chromium pigments, Br. J. Ind. Med., 32, (1975) pp. 62
[5] A. Sheffet, I. Thind, A. M. Miller, D. B. Louria, Cancer mortality in a pigment plant utilizing lead and zinc chromates, Arch. Environ. Health, 37, (1982), pp. 44-52
[6] R. Berger, U. Bexell, T.M. Grehk, S.E. Hornstrom, A comparative study of the corrosion protective properties of chromium and chromium free passivation methods, Surf. Coat. Technol., 202, (2007), pp. 391-397
[7] M.F. Montemor, Functional and smart coatings for corrosion protection: a review of recent advances, Surf. Coat. Technol., 258, (2014), pp. 17-37
[8] P. Puomi, H.M. Fagerholm, J.B. Rosenholm, K. Jyrkas, Comparison of different commercial pretreatment methods for hot-dip galvanized and Galfan coated steel, Surf. Coat. Technol., 115, (1999), pp. 70-78
[9] P. Puomi, H.M. Fagerholm, A. Sopanen, Parameters affecting long-term performance of painted galvanized steels, Anti Corros. Methods Mater., 48, (2001), pp. 160-171
[10] G. Williams, H.N. McMurray Chromate inhibition of corrosion-driven organic coating delamination studied using a scanning Kelvin probe technique, J. Electrochem. Soc., 148, (2001), pp. B337-B385
[11] Y. L. Kuznetsov, I. L. Rosenfeld, T. A. Agalarova, Protection of steel in seawater by chromate inhibitors in conjunction with cathodic polarization, Prot. Met., 18, (1982), p. 438.
[12] I. L. Rosenfeld, Corrosion Inhibitors, McGraw Hill: New York, (1981) p. 145.
[13] J. Zhao, G. Frankel, R. L. McCreery, Corrosion Protection of Untreated AA-2024-T3 in Chloride Solution by a Chromate Conversion Coating Monitored with Raman Spectroscopy J. Electrochem. Soc. 145, (1998), 2258-2264.
[14] US Army Research Laboratory: Pauline Smith, Kestutis Chesonis, Christopher Miller and John Escarsega, Final Report on Alternative Chrome-free Wash Primers, Army Research Laboratory, Aberdeen Proving Ground, September 2006, ARL-TR-3932 MD 21005-5069
[15] NIIR Board. Modern Technology of Paints, Varnished & Lacquers, Vinyl Resins for Coatings, Asia Pacific Business Press Inc. 2007, p. 487-490, 2nd edition.
[16] S. Bohm, H.N. McMurray, S.M. Powell, D.A. Worsley, Novel environment friendly corrosion inhibitor pigments based on naturally occurring clay minerals Mater. Corros., 52 (2001), pp. 896-903
[17] G. Williams, H.N. McMurray, D.A. Worsley, Cerium (III) inhibition of corrosion driven organic coating delamination studied using a scanning Kelvin probe technique J. Electrochem. Soc., 149 (2002), pp. B154-B162
[18] R.G. Buchheit, H. Guan, S. Mahajanam, F. Wong, Active corrosion protection and corrosion sensing in chromate-free organic coatings, Prog. Org. Coat., 47 (2003), pp. 174-182
[19] S. E. Karekar, U. D. Bagale, S. H. Sonawane, B. A. Bhanvase, & D. V. Pinjari, A smart coating established with encapsulation of Zinc Molybdate centred nanocontainer for active corrosion protection of mild steel: release kinetics of corrosion inhibitor. Composite Interfaces, 25(9), (2018), pp. 785–808.
[20] M. Finšgar, & I. Milošev. Inhibition of copper corrosion by 1,2,3-benzotriazole: A review. Corrosion Science, 52(9), (2010), pp. 2737–2749.
[21] N. Kovačević, & A. Kokalj, Chemistry of the interaction between azole type corrosion inhibitor molecules and metal surfaces. Materials Chemistry and Physics, 137(1), (2012), pp. 331–339.

[22] K. Xhanari, & M. Finšgar. Organic corrosion inhibitors for aluminum and its alloys in chloride and alkaline solutions: A review. Arabian Journal of Chemistry, (2016)
[23] T. J. Harvey, F. C. Walsh, & A.H. Nahlé, A review of inhibitors for the corrosion of transition metals in aqueous acids. Journal of Molecular Liquids, 266, (2018), pp. 160–175.
[24] G. Williams, & H. N. Mcmurray, Inhibition of filiform corrosion on organic-coated AA2024-T3 by smart-release cation and anion-exchange pigments. Electrochem. Acta, 69, (2012), pp. 287–294.
[25] G. Markevicius, S. Chaudhuri, C. Bajracharya, R. Rastogi, J. Xiao, C. Burnett, T.Q. Chastek, Polyoligomeric silsesquioxane (POSS)–hydrogenated polybutadiene polyurethane coatings for corrosion inhibition of AA2024, Progress in Organic Coatings, 75 (2012) pp. 319-327
[26] M. Serdechnova, A. N. Salak, F. S. Barbosa, D. E.L. Vieira, J. Tedim, M. L. Zheludkevich and M. G. S. Ferreira, Interlayer intercalation and arrangement of 2-mercaptobenzothiazolate and 1,2,3-benzotriazolate anions in layered double hydroxides: In situ X-ray diffraction study, Journal of Solid State Chemistry, 233 (2016) pp. 158-165
[27] N. Cotolan, S. Varvara, E. Albert, G. Szabó, Z. Hórvölgyi & L.-M. Mureşan, Evaluation of corrosion inhibition performance of silica sol–gel layers deposited on galvanised steel, Corrosion Engineering, Science and Technology, 51, (2016) pp. 373-382
[28] K. Kamburova, N. Boshkova, N. Boshkov & Ts. Radeva, Design of polymeric core-shell nanocontainers impregnated with benzotriazole for active corrosion protection of galvanized steel, Colloids and Surfaces A: Physicochemical and Engineering Aspects, Vol. 499, (2016) pp. 24-30
[29] B. Ramezanzadeh, E. Ghasemi, F. Askari & M. Mahdavian, Synthesis and characterization of a new generation of inhibitive pigment based on zinc acetate/benzotriazole: Solution phase and coating phase studies, Dyes and Pigments, 122 (2015) pp. 331-345
[30] J. E. Fagel Jr., G. W. Ewing, The Ultraviolet Absorption of Benzotriazole J. Am. Chem. Soc., 73 (9), (1951), pp. 4360–4362
[31] M. Stratmann, R. Feser, and A. Leng, Corrosion protection by organic films, Electrochim. Acta, 39, (1994) pp. 1207-1214
[32] A. Leng, H. Streckel, M. Stratmann, The delamination of polymeric coatings from steel. Part 1: calibration of the Kelvin probe and basic delamination mechanism, Corros. Sci., 41 (1999), pp. 547-578
[33] W. Furbeth and M. Stratmann, Scanning Kelvin probe investigations on the delamination of polymeric coatings from metallic surfaces, Prog. Org. Coat., 39, (2000) pp. 23-29
[34] https://www.sigmaaldrich.com/chemistry/chemical-synthesis/learning-center/technical-bulletins/al-142/amberlite-amberlyst.html last accessed December the 9th, 2018
[35] M. Pourbaix, N. de Zoubov, in: M. Pourbaix (Ed.), Atlas of Electrochemical Equilibria in Aqueous Solution, Pergamon Press, (1966), p. 406
[36] H.S. Wroblowa, S.B. Qaderi, The mechanism of oxygen reduction on steel, J. Electroanal. Chem. 279 (1990) pp. 231-242.
[37] H.S. Wroblowa, S.B. Qaderi, The mechanism of oxygen reduction on zinc, J. Electroanal. Chem. 295 (1990) pp. 153-161.
[38] H. Dafydd, D. A. Worsley, and H. N. McMurray, Corrosion Science, 47(12), (2005), pp. 3006-3018
[39] M. Stratmann, A. Leng, W. Fürbeth, H. Streckel, H. Gehmecker, K.-H. Groβe-Brinkhaus, The scanning Kelvin probe; a new technique for the in situ analysis of the delamination of organic coatings, Prog. Org. Coat., 27 (1996), pp. 261-267
[40] W. Furbeth, M. Stratmann, The delamination of polymeric coatings from electrogalvanized steel - a mechanistic approach. Part 2: delamination from a defect down to steel, Corros. Sci., 43 (2001), pp. 229-241
[41] H. Dominighaus, Plastics for Engineers, Hanser Publications, Munich (1988), p. 142
[42] R.J. Holness, G. Williams, D.A. Worsley, H.N. McMurray, Polyaniline inhibition of corrosion-driven organic coating cathodic delamination on iron, J. Electrochem. Soc., 152 (2005), p. B73-B81
[43] C. F. Glover, C. A. J. Richards, G. Williams, & H. N. McMurray, Evaluation of multi-layered

graphene nano-platelet composite coatings for corrosion control part II – Cathodic delamination kinetics. Corrosion Science 136, (2018), pp. 304-310
[44] J. V. Custódioa, S. M. L. Agostinhoa, A. M.P. Simõesb, Electrochemistry and surface analysis of the effect of benzotriazole on the cut edge corrosion of galvanized steel, Electrochimica Acta 55 (2010) pp. 5523–5531
[45] A. Kokalj, Ab initio modelling of the bonding of benzotriazole corrosion inhibitor to reduced and oxidized copper surfaces, Faraday Discuss., 180, (2015), pp. 415-438
[46] N. K. Allam, A. A. Nazeer & E. A. Ashour, A review of the effects of benzotriazole on the corrosion of copper and copper alloys in clean and polluted environments, J Appl Electrochem 39, (2009) pp. 961–969
[47] N. K. Allam, A. A. Nazeer & E. A. Ashour, A review of the effects of benzotriazole on the corrosion of copper and copper alloys in clean and polluted environments, J Appl Electrochem 39 (2009) pp. 961–969
[48] A. Frigani, M. Fonsati, C. Monticelli, G. Brunoro, Influence of the alkyl chain on the protective effects of 1,2,3-benzotriazole towards copper corrosion.: Part I: inhibition of the anodic and cathodic reactions, Corros Sci, 41, (1999) pp. 1205-1215
[49] S. Mamas, T. Kıyak, M. Kabasakaloglu & A. Koc, The effect of benzotriazole on brass corrosion, Materials Chemistry and Physics 93 (2005) pp. 41–47
[50] J. Rodriguez, M. Mouanga, A. Roobroeck, D. Cossement, A. Mirisola, M.-G. Olivier, Study of the inhibition ability of benzotriazole on the Zn-Mg coated steelcorrosion in chloride electrolyte, Corrosion Science 132 (2018) pp. 56–67
[51] J. B. Cotton, The Control of Surface Reactions on Copper by Means of Organic Reagents. Proceedings of the 2nd Inter. Congress on Metallic Corrosion, New York, (1963) pp. 590–596
[52] R. Youda, H. Nishihara, K. Aramaki, SERS and impedance study of the equilibrium between complex formation and adsorption of benzotriazole and 4-hydroxybenzotriazole on a copper electrode in sulphate solutions, Electrochim Acta, 35(6) (1990) pp. 1011-1017
[53] E. Kondoh, T. Kawakami, M. Watanabe, L. Jin, S. Hamada, S. Shima, and H. Hiyama, Structures of Cu surfaces developing in benzotriazole solutions: Effect of pH, Japanese Journal of Applied Physics 56, (2017), 07KH01

7. Figures

Figure 1: A plot displaying the relative concentration of benzotriazole species as a function of pH.

Figure 2: An illustrated schematic of the a) uptake proton transfer reaction of BTAH from solution by the exchange resin, and b) the release reaction of the $BTAH_2^+$ from the resin and the subsequent deprotonation of said species to the anionic BTA^- when in a high pH environment.

Figure 3: A plot showing the measured [BTA^-] concentration over log time throughout the uptake reaction.

Figure 4: Schematic representation of the corrosion-driven cathodically delaminating cell showing correspondence with various regions of the time-dependent $E_{corr}(x)$ profile.

Figure 5: E_{intact} vs time plots for HDG zinc surfaces coated with PVB films containing CBP volume fractions (Φ) of a) 0, b) 0.01, c) 0.025, d) 0.05 and e) 0.1, measured over 20 hours.

Figure 6: Plots of the time-dependent E_{corr} vs. delamination distance profiles recorded for PVB containing Φ_{CBP} equal to a) 0, b) 0.01 and c) 0.1 coated on HDG steel substrates shown at 2 hour intervals for a) and 4 hour intervals for b) and c), commencing at 2 hours post initiation and ending after 24 hours. Delamination was initiated with 0.86 M NaCl.

Figure 7: Plots of delamination distance (x_{del}) as a function time (t_{del} - t_i) for PVB films containing CBP volume fractions (Φ) of a) 0, b) 0.01, c) 0.025, d) 0.05 and e) 0.1.

Figure 8: Plots of the normalised delamination rates as a function of pigment volume fraction for both a) PVB coatings containing CBP and b) PVB coatings containing strontium chromate.

Figure 9: Showing the measured [BTA^-] concentration over time for each 'release' wash, where a) represents the first wash, b) the second and c) the third.

Figure 10: A plot of the cathodic-going polarization curves (linear potential sweep rate of 3.3 $\times 10^{-4}$ Vs^{-1} and a rotation head speed of 217 rad s^{-1}) obtained for zinc HDG steel surfaces where the solution electrolyte (0.5 M aqueous sodium sulfate containing 0.05 M sodium tetraborate ($Na_2B_4O_7.10H_2O$) and 0.1 M sodium hydroxide (NaOH)) concentration of BTA for each curve was a) zero, b) 2 x 10^{-5} M, c) 2 x 10^{-4} M, d) 2 x 10^{-3} M and e) 2 x 10^{-2} M.

Figure 11: Showing the obtained OCP and Rp values, taken from Fig. 10, plotted as a function of [BTA^-] concentration. Rp values were calculated by taking the reciprocal gradient of the tangent to the I vs E curve and constructed at OCP (I = zero) found in Fig. 10.

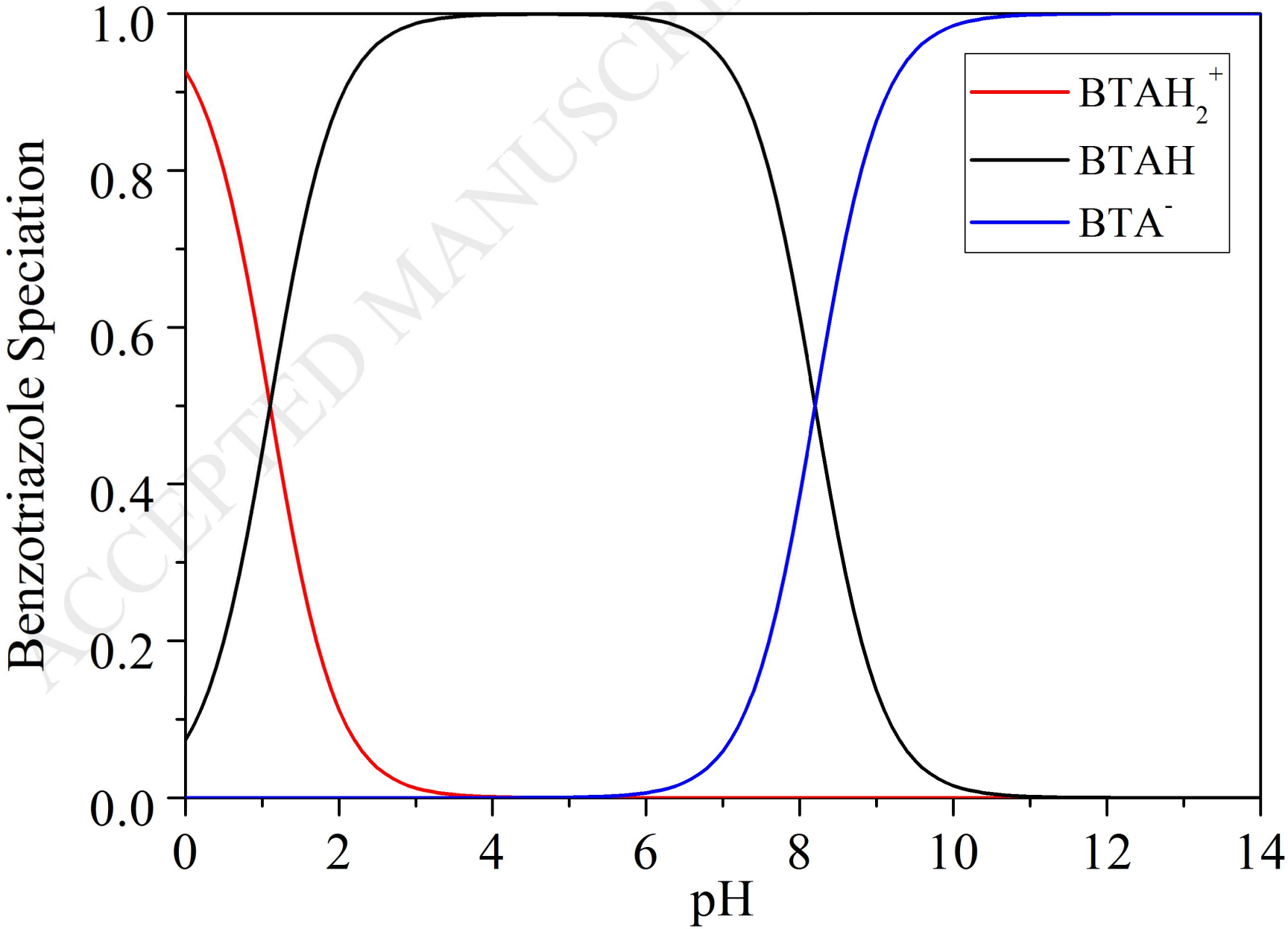

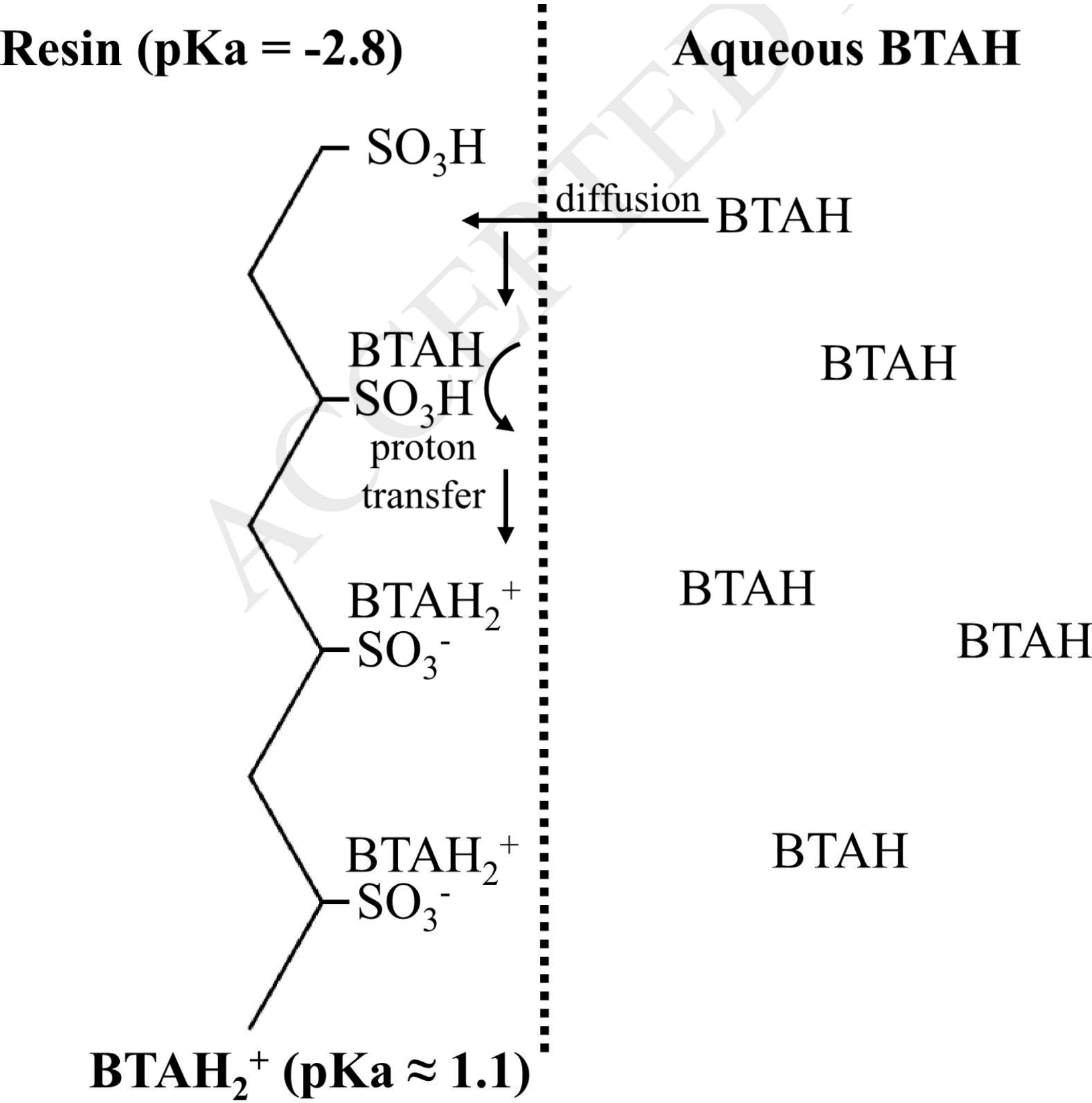
Resin (pKa = -2.8)
Aqueous BTAH
SO3H
diffusion
BTAH
BTAH
SO3H
BTAH
proton
transfer
BTAH2+
SO3-
BTAH
BTAH
BTAH2+
SO3-
BTAH
BTAH2+ (pKa ≈ 1.1)

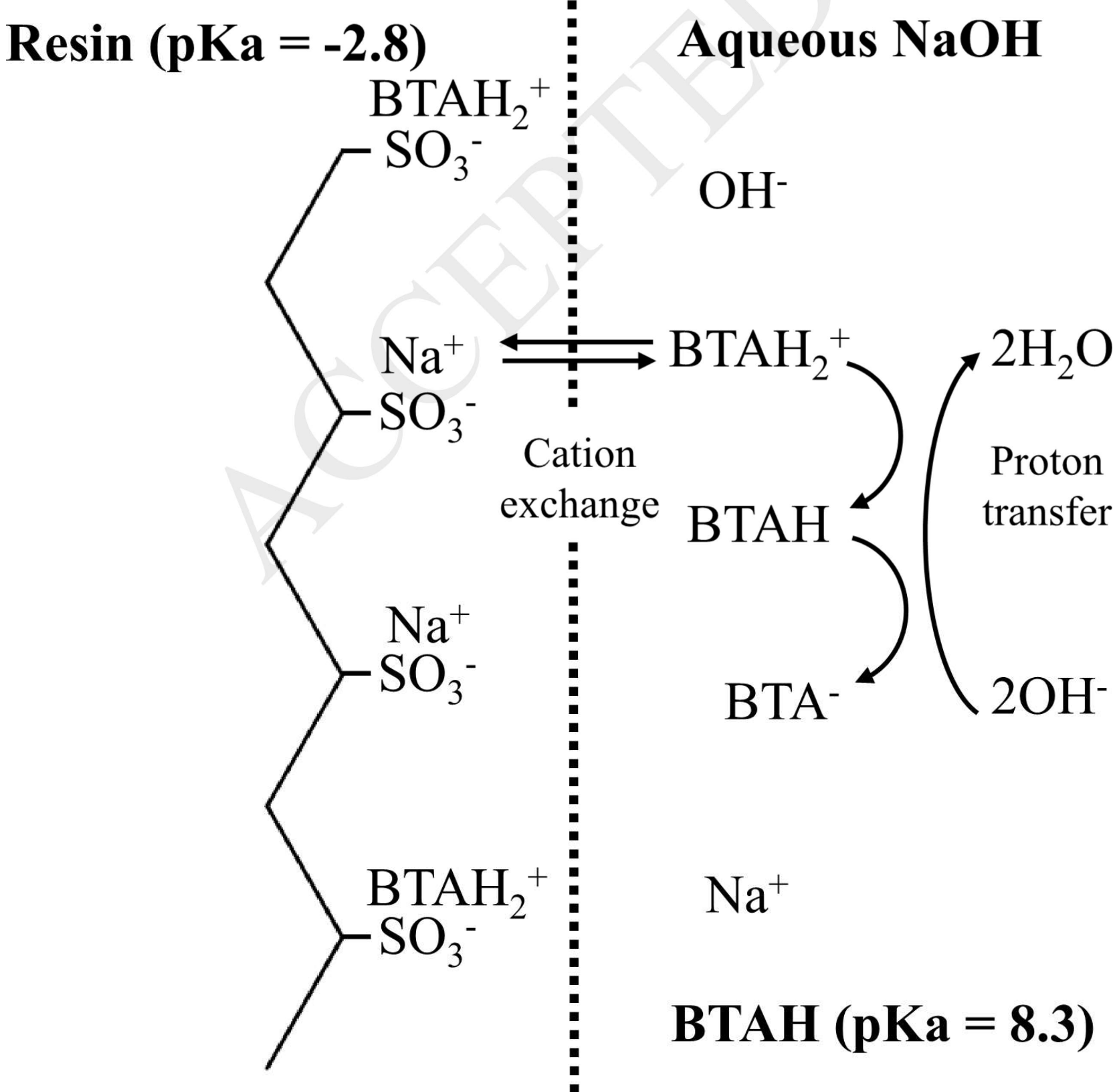
Resin (pKa = -2.8)
Aqueous NaOH
BTAH2+
SO3-
OH-
Na+
SO3-
BTAH2+
2H2O
Cation
exchange
BTAH
Proton
transfer
Na+
SO3-
BTA-
2OH-
BTAH2+
SO3-
Na+
BTAH (pKa = 8.3)

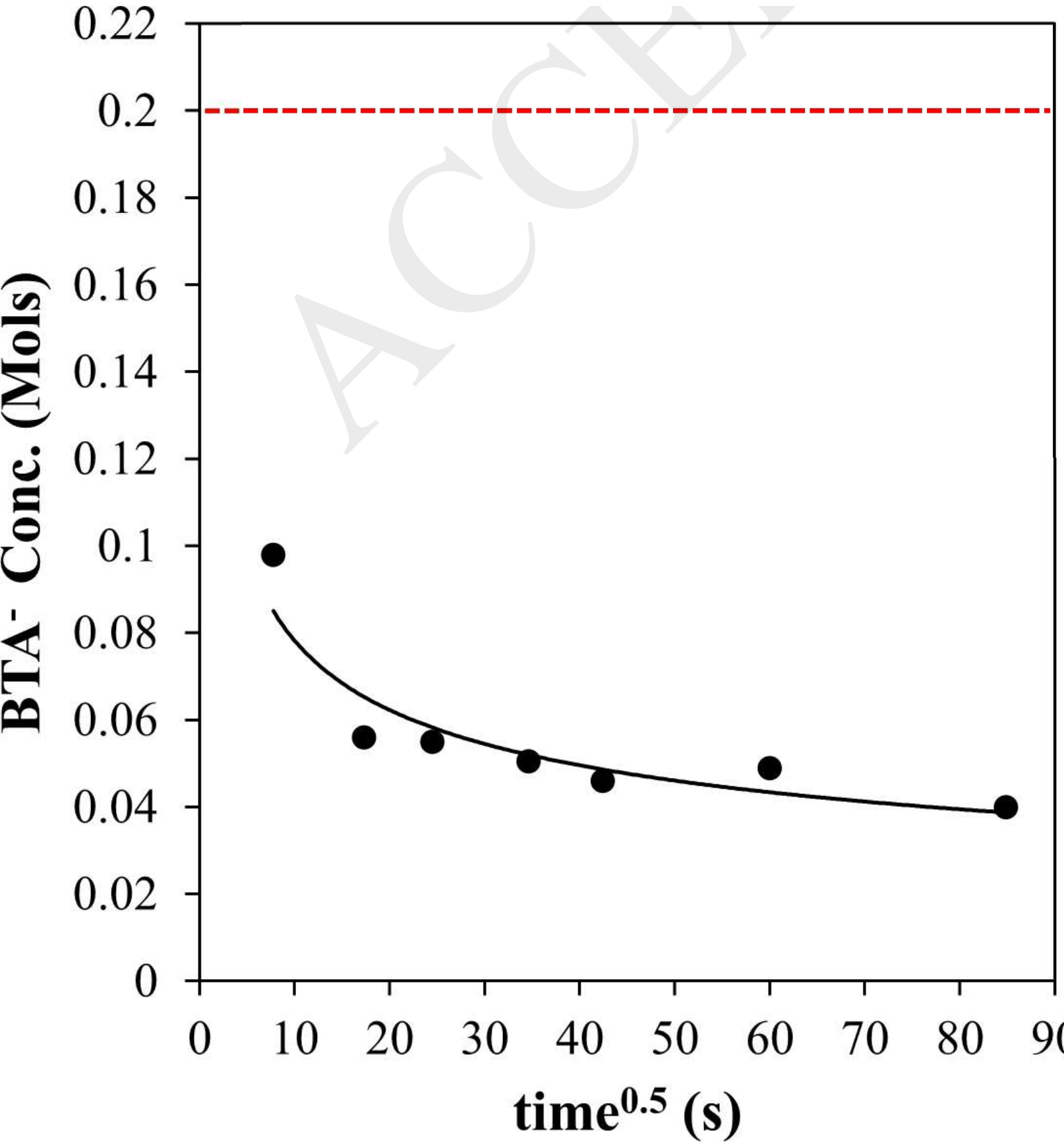
0.22
0.2
0.18
0.16
0.14
0.12
0.1
0.08
0.06
0.04
0.02
0
BTA- Conc. (Mols)
0
10
20
30
40
50
60
70
80
90
time0.5 (s)

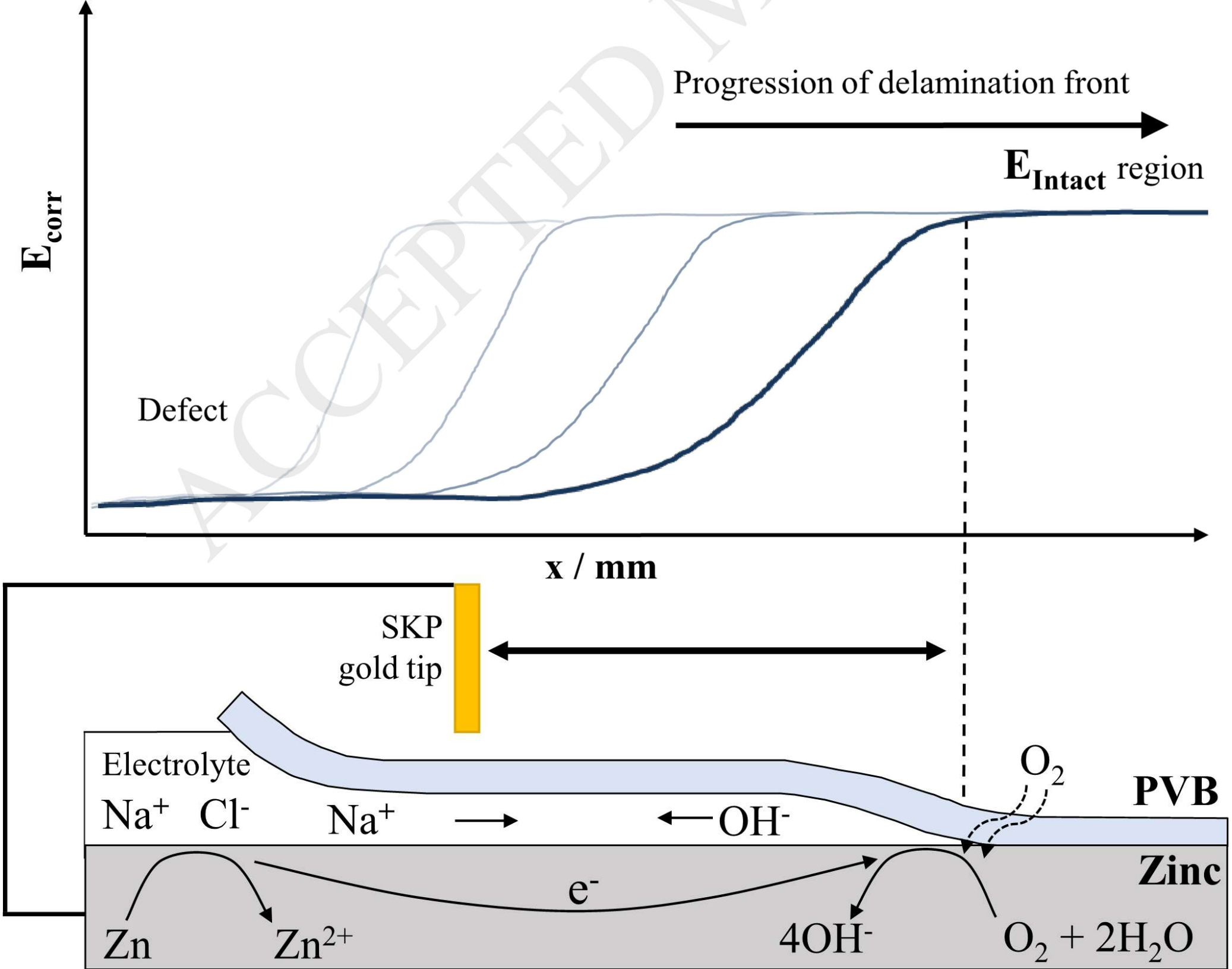

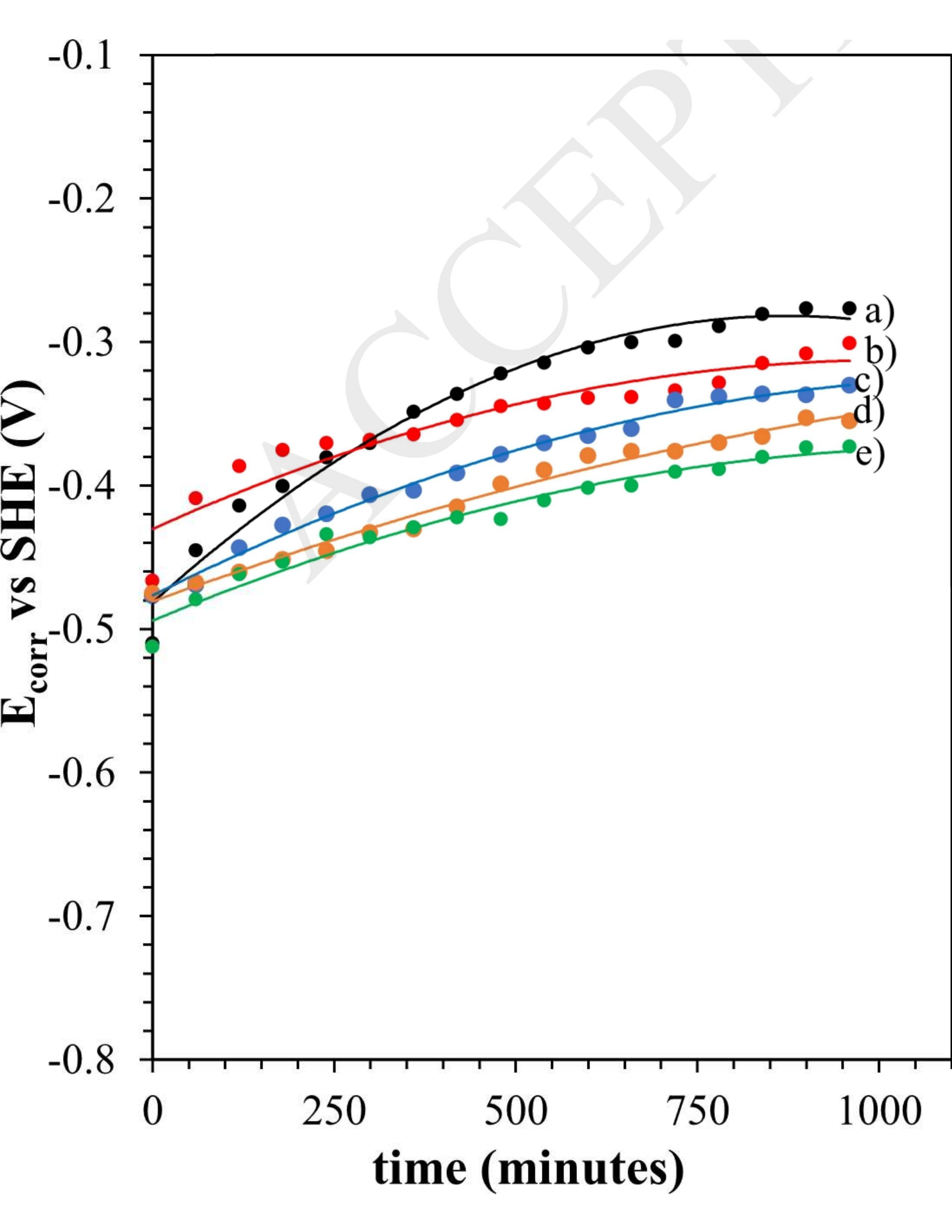
-0.1
-0.2
-0.3
-0.4
-0.5
-0.6
-0.7
-0.8
E_{corr} vs SHE (V)
0
250
500
750
1000
time (minutes)
a)
b)
c)
d)
e)

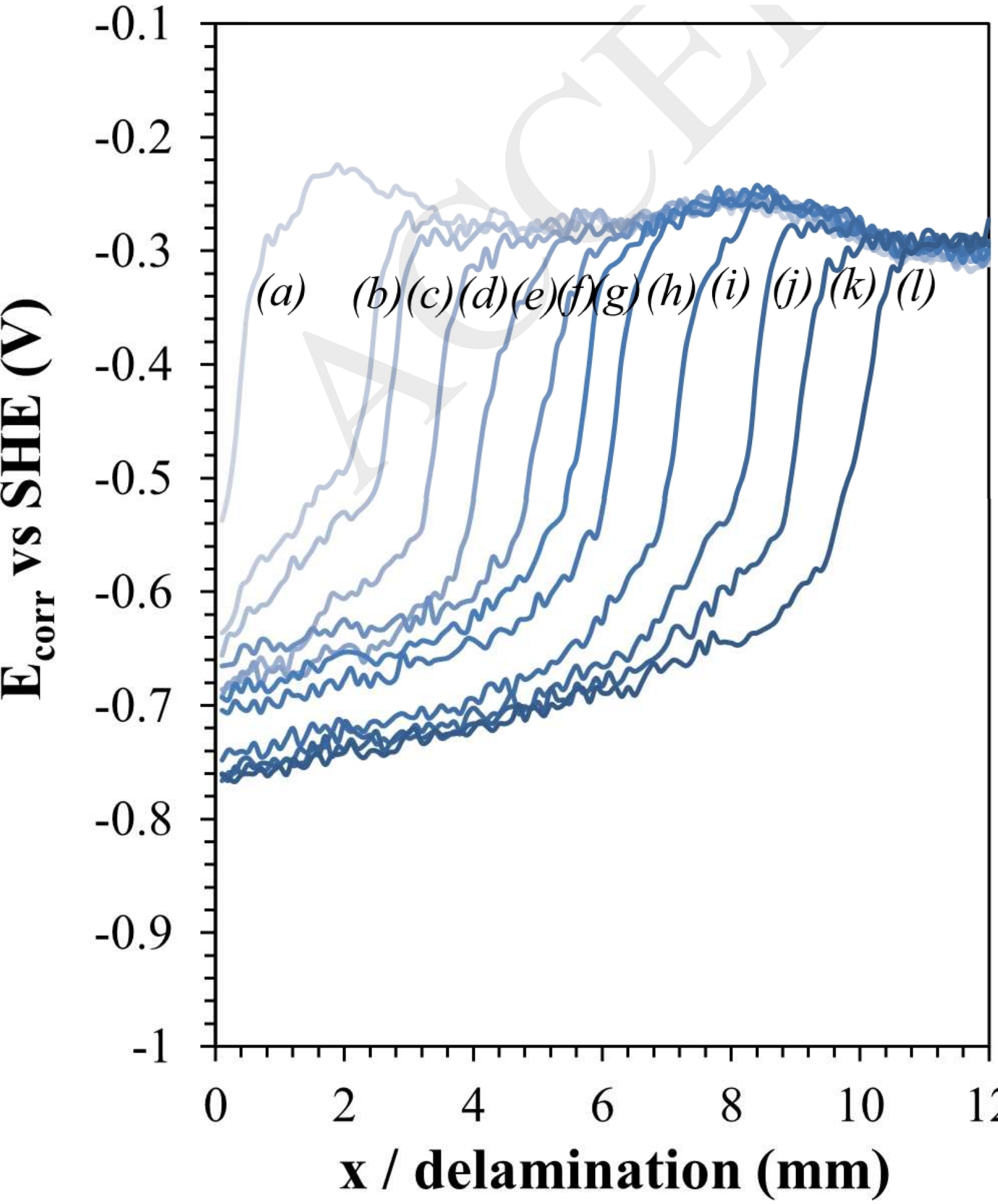
-0.1
-0.2
-0.3
-0.4
-0.5
-0.6
-0.7
-0.8
-0.9
-1
E_corr vs SHE (V)
(a)
(b)
(c)
(d)
(e)
(f)
(g)
(h)
(i)
(j)
(k)
(l)
0
2
4
6
8
10
12
x / delamination (mm)

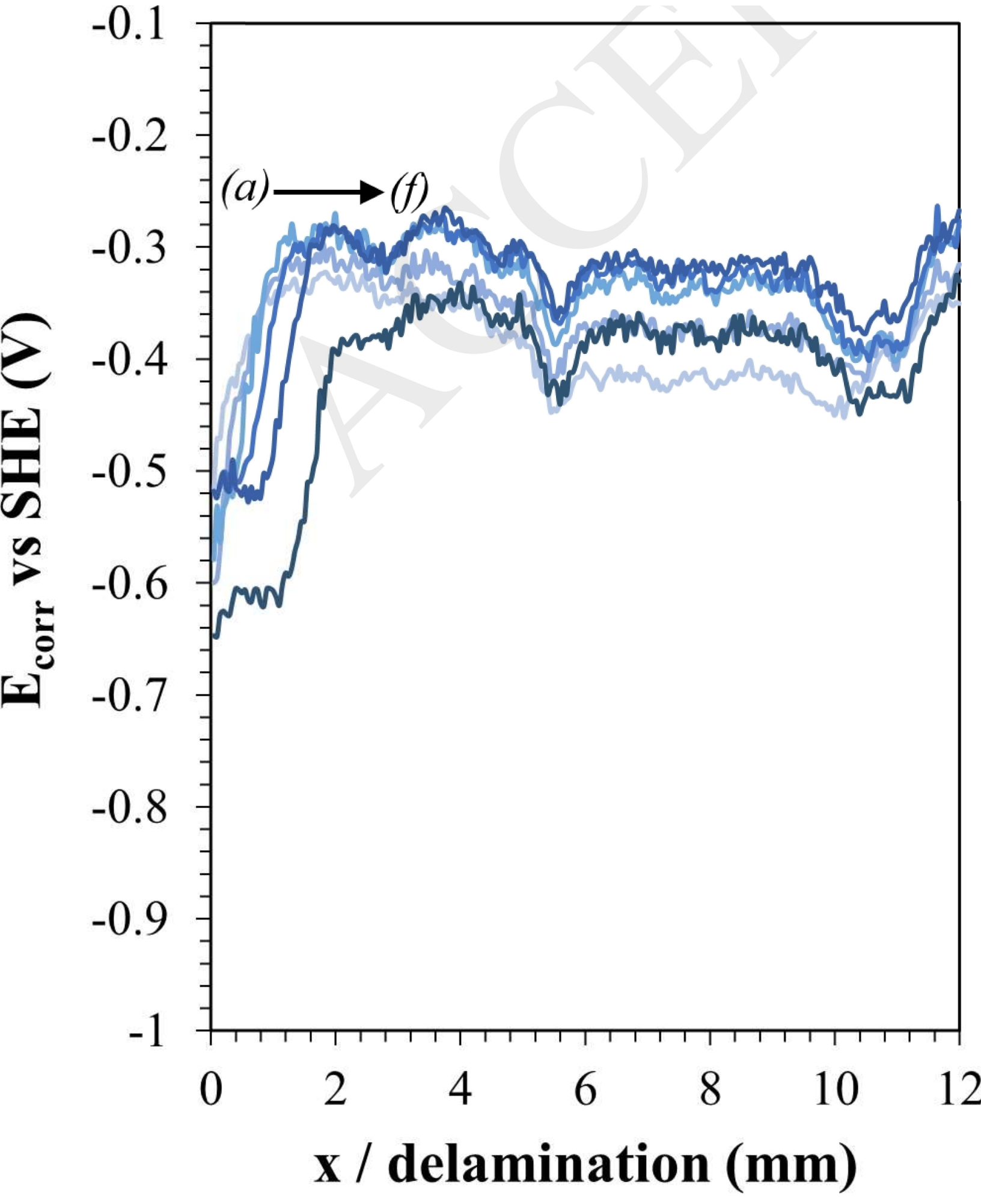
-0.1
-0.2
-0.3
-0.4
-0.5
-0.6
-0.7
-0.8
-0.9
-1
(a)
(f)
E_corr vs SHE (V)
0
2
4
6
8
10
12
x / delamination (mm)

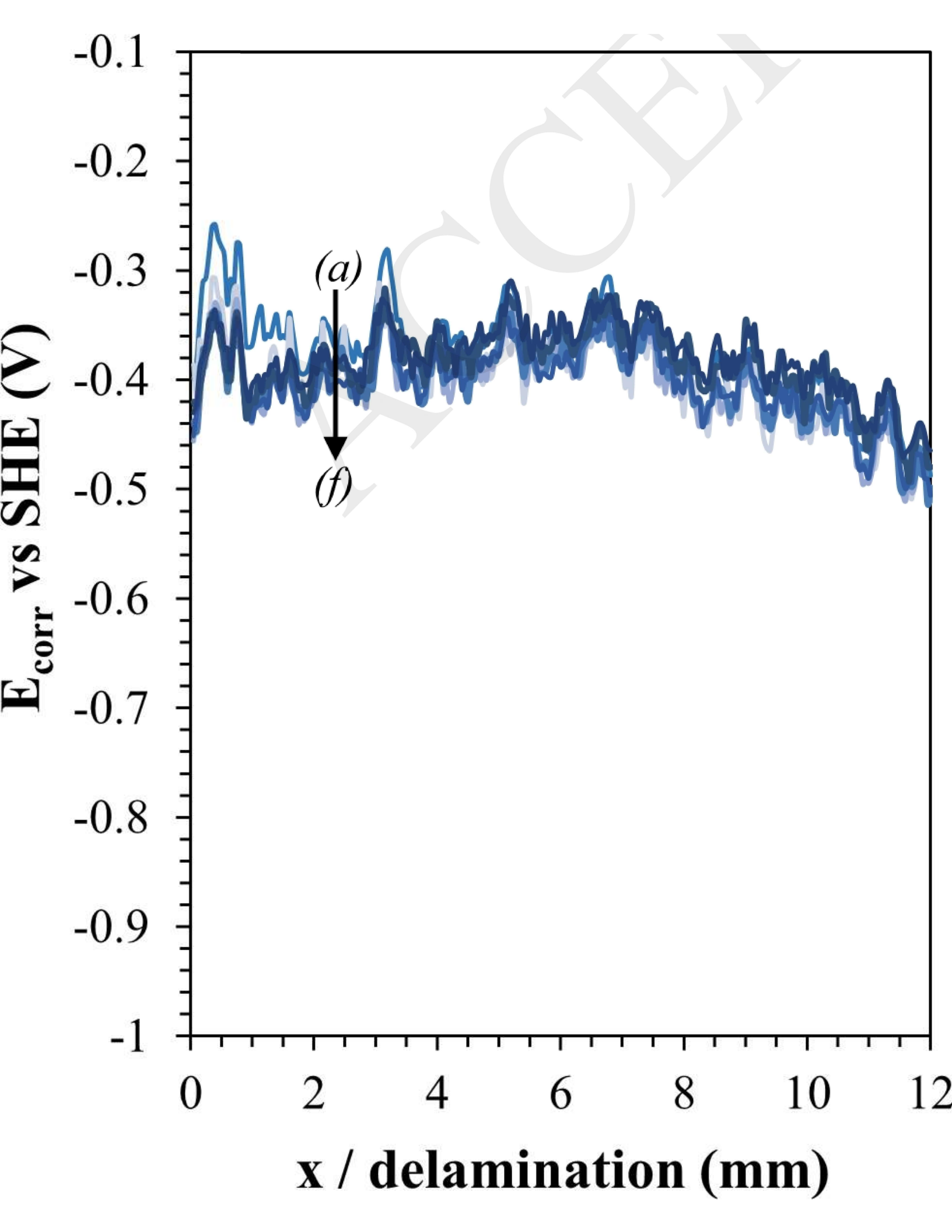
-0.1
-0.2
-0.3
-0.4
-0.5
-0.6
-0.7
-0.8
-0.9
-1
(a)
(f)
E_corr vs SHE (V)
0
2
4
6
8
10
12
x / delamination (mm)

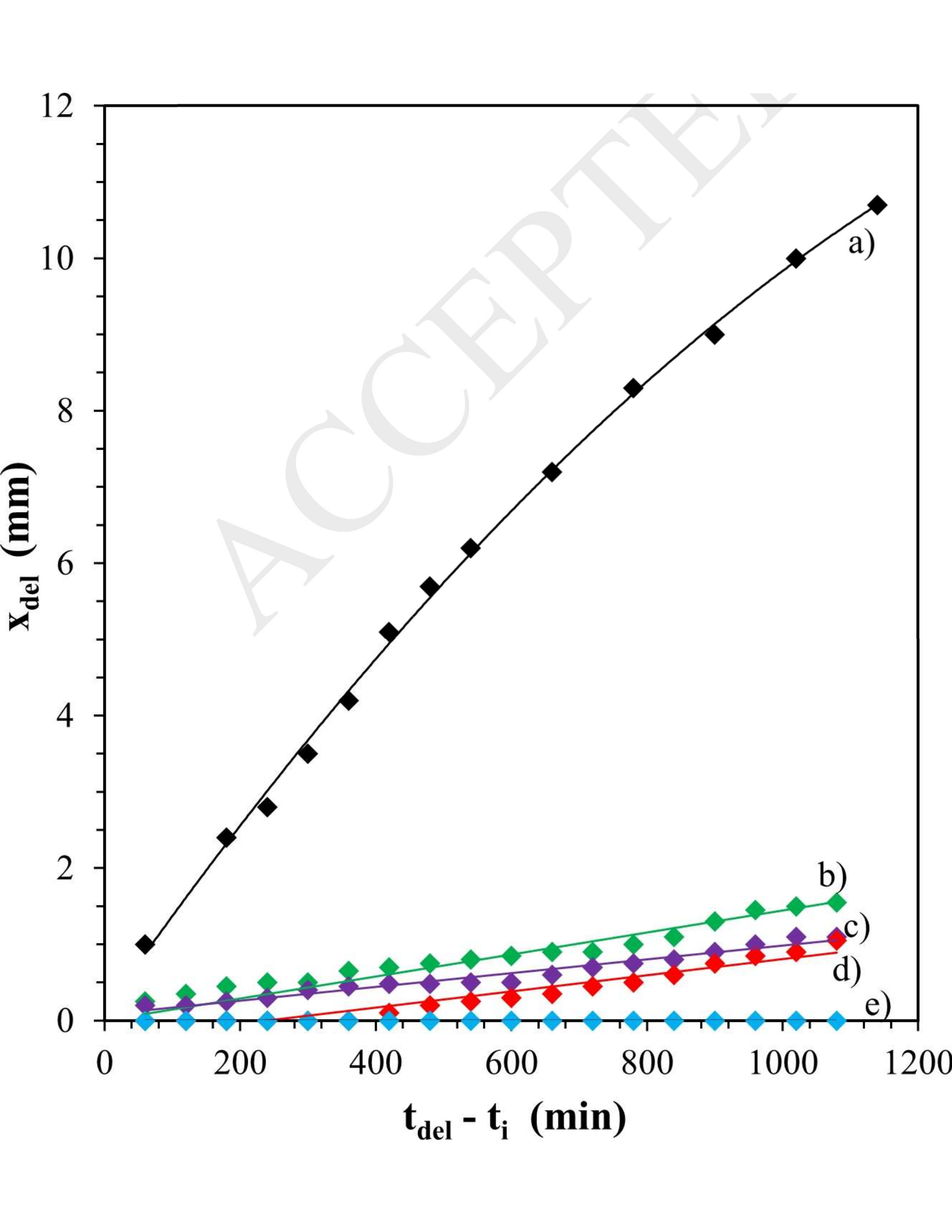
12
10
8
6
4
2
0
x_{del} (mm)
0
200
400
600
800
1000
1200
$t_{del} - t_i$ (min)
a)
b)
c)
d)
e)

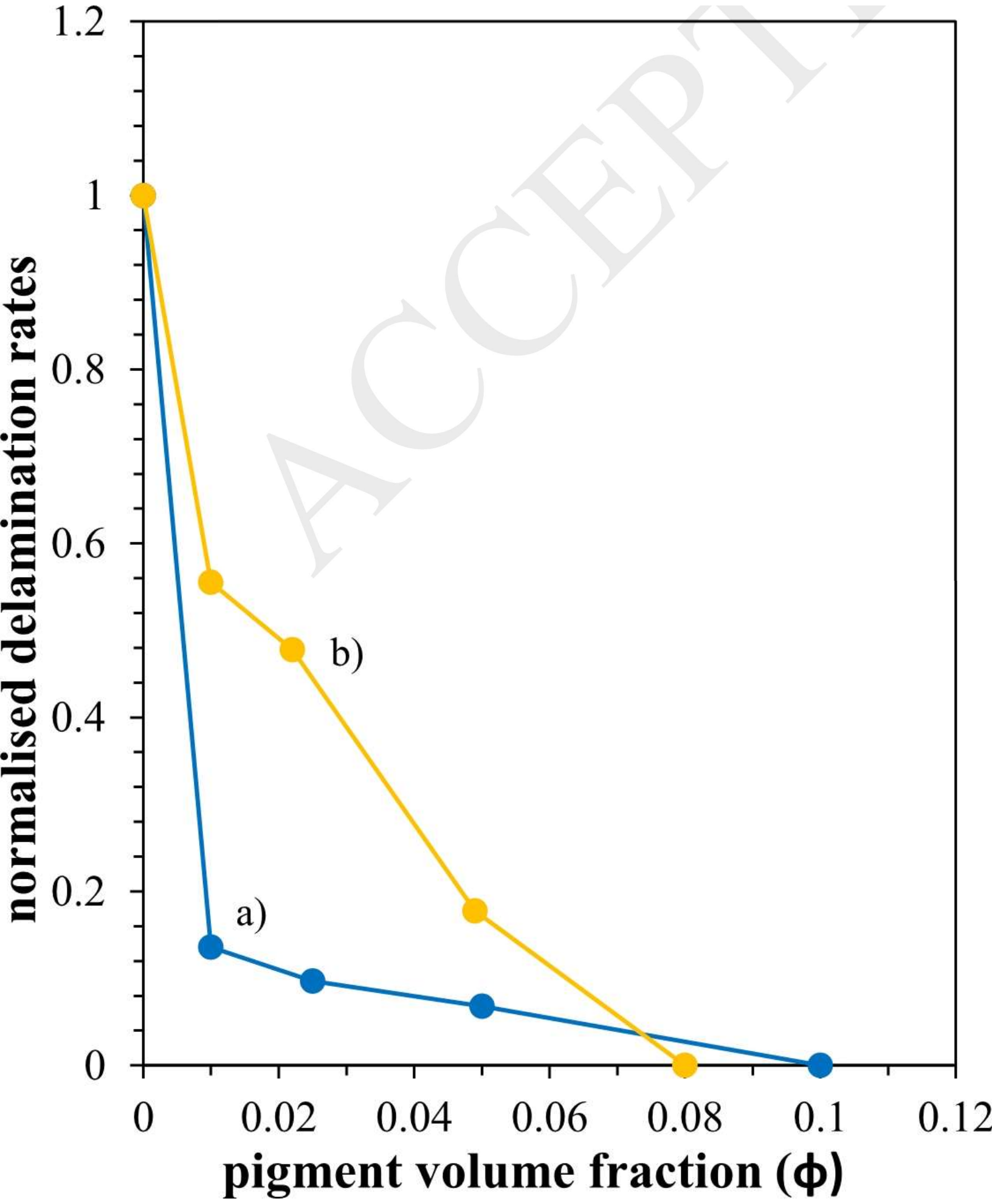
1.2
1
0.8
0.6
0.4
0.2
0
normalised delamination rates
0
0.02
0.04
0.06
0.08
0.1
0.12
pigment volume fraction (ϕ)
a)
b)

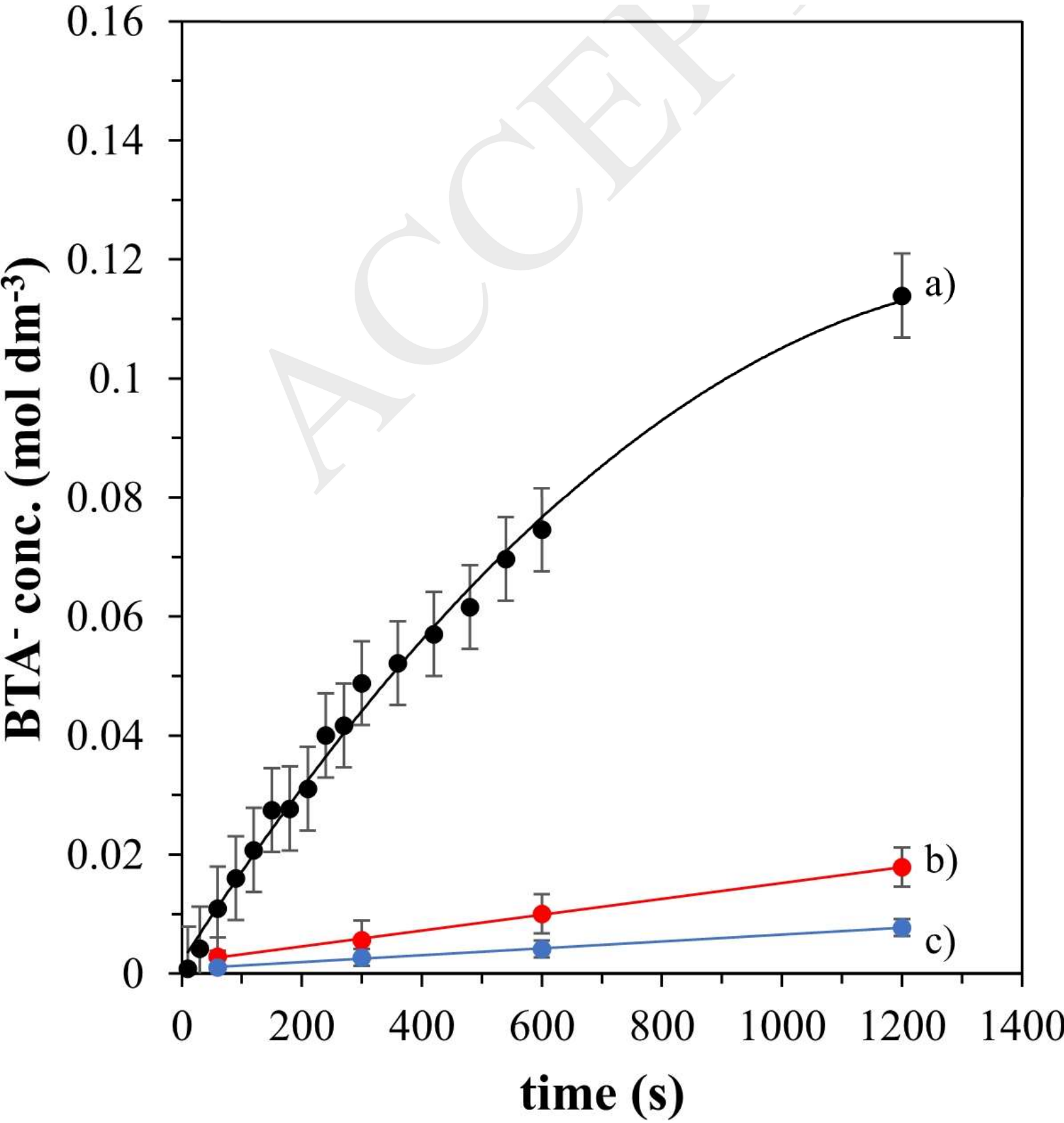
0.16
0.14
0.12
0.1
0.08
0.06
0.04
0.02
0
BTA- conc. (mol dm-3)
a)
b)
c)
0
200
400
600
800
1000
1200
1400
time (s)

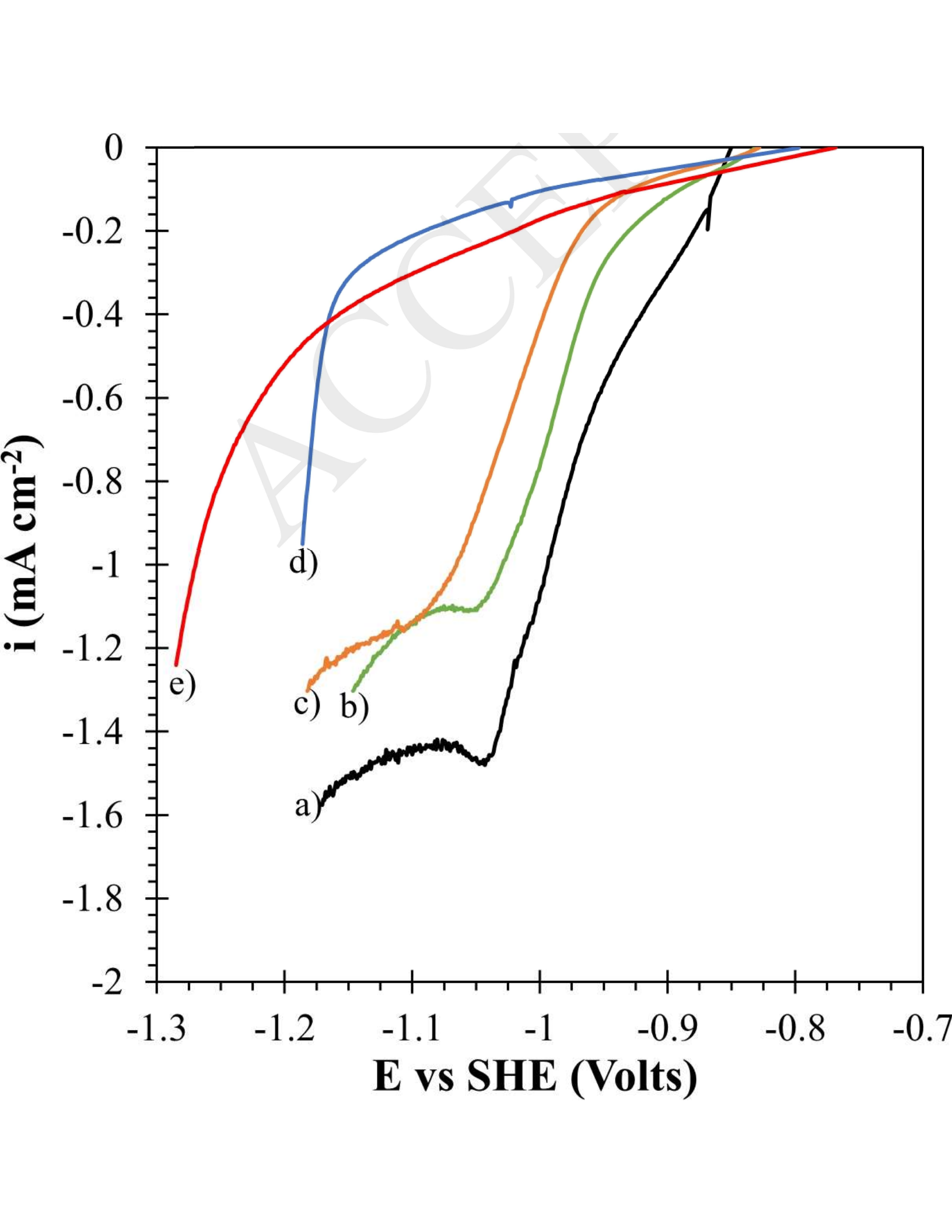
0
-0.2
-0.4
-0.6
-0.8
-1
-1.2
-1.4
-1.6
-1.8
-2
i (mA cm-2)
-1.3
-1.2
-1.1
-1
-0.9
-0.8
-0.7
E vs SHE (Volts)
a)
b)
c)
d)
e)

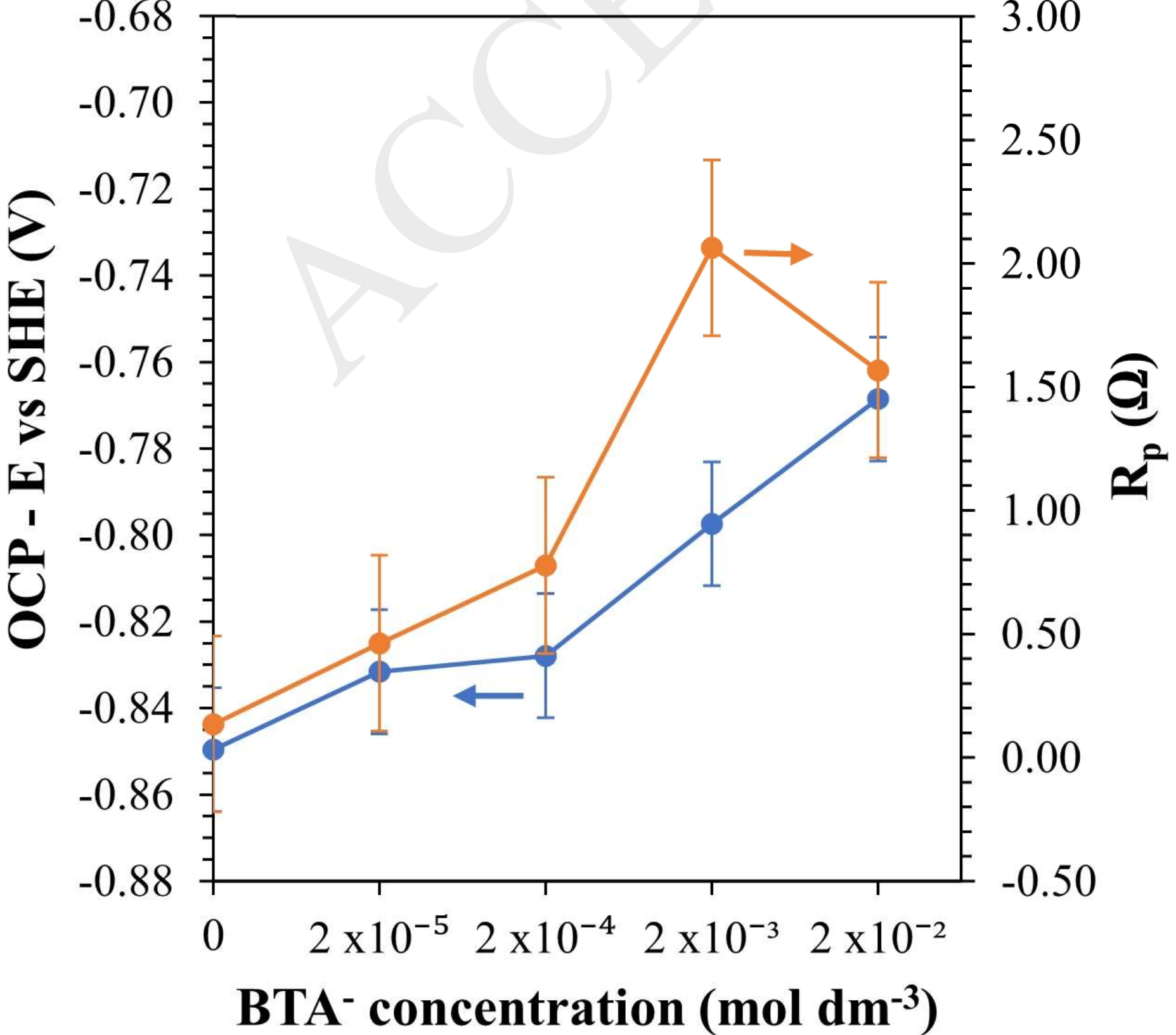
-0.68
-0.70
-0.72
-0.74
-0.76
-0.78
-0.80
-0.82
-0.84
-0.86
-0.88
OCP - E vs SHE (V)
3.00
2.50
2.00
1.50
1.00
0.50
0.00
-0.50
R_p (Ω)
0
2 x10⁻⁵
2 x10⁻⁴
2 x10⁻³
2 x10⁻²
BTA⁻ concentration (mol dm⁻³)